

WISE/NEOWISE Multi-Epoch Imaging of the Potentially Geminid-related Asteroids: (3200) Phaethon, 2005 UD and 1999 YC

TOSHIHIRO KASUGA¹ AND JOSEPH R. MASIERO²

¹*National Astronomical Observatory of Japan, 2-21-1 Osawa, Mitaka, Tokyo 181-8588, Japan*

²*Caltech/IPAC, 1200 E California Blvd, MC 100-22, Pasadena, CA 91125, USA*

(Accepted for publication in The Astronomical Journal)

ABSTRACT

We present space-based thermal infrared observations of the presumably Geminid-associated asteroids: (3200) Phaethon, 2005 UD and 1999 YC using *WISE*/NEOWISE. The images were taken at the four wavelength bands $3.4\mu\text{m}$ (*W1*), $4.6\mu\text{m}$ (*W2*), $12\mu\text{m}$ (*W3*), and $22\mu\text{m}$ (*W4*). We find no evidence of lasting mass-loss in the asteroids over the decadal multi-epoch datasets. We set an upper limit to the mass-loss rate in dust of $Q_{\text{dust}} \lesssim 2\text{ kg s}^{-1}$ for Phaethon and $\lesssim 0.1\text{ kg s}^{-1}$ for both 2005 UD and 1999 YC, respectively, with little dependency over the observed heliocentric distances of $R_{\text{h}}=1.0\text{--}2.3\text{ au}$. For Phaethon, even if the maximum mass-loss was sustained over the 1000(s)yr dynamical age of the Geminid stream, it is more than two orders of magnitude too small to supply the reported stream mass ($10^{13\text{--}14}\text{ kg}$). The Phaethon-associated dust trail (Geminid stream) is not detected at $R_{\text{h}}=2.3\text{ au}$, corresponding an upper limit on the optical depth of $\tau < 7\times 10^{-9}$. Additionally, no co-moving asteroids with radii $r_{\text{e}} < 650\text{ m}$ were found. The DESTINY⁺ dust analyzer would be capable of detecting several of the $10\mu\text{m}$ -sized interplanetary dust particles when at far distances ($\gtrsim 50,000\text{ km}$) from Phaethon. From 2005 UD, if the mass-loss rate lasted over the 10,000yr dynamical age of the Daytime Sextantid meteoroid stream, the mass of the stream would be $\sim 10^{10}\text{ kg}$. The 1999 YC images showed neither the related dust trail (the optical depth $\tau < 2\times 10^{-8}$) nor co-moving objects with radii $r_{\text{e}} < 170\text{ m}$ at $R_{\text{h}}=1.6\text{ au}$. Estimated physical parameters from these limits do not explain the production mechanism of the Geminid meteoroid stream. Lastly, to explore the origin of the Geminids, we discuss the implications for our data in relation to the possibly Sodium (Na)-driven perihelion activity of Phaethon.

Keywords: Solar system astronomy; Meteors; Asteroids; Near-Earth objects; Surveys; Catalogs

Corresponding author: Toshihiro Kasuga
toshi.kasuga@nao.ac.jp

1. INTRODUCTION

The near-Earth asteroid (NEA) (3200) Phaethon (hereafter just Phaethon) appears to be dynamically associated with the Geminid meteoroid stream ¹ (Whipple 1983; Gustafson 1989; Williams & Wu 1993). The semimajor axis $a=1.271$ au, eccentricity $e=0.890$, and inclination $i=22^\circ.3$ (NASA JPL HORIZONS²) corresponds to a Tisserand parameter $T_J = 4.5$, which is distinctly above those of cometary orbits ($T_J \leq 3.08$) and is classified as having a typical asteroidal orbit (Jewitt & Hsieh 2022). The Geminid meteoroid stream consists of near millimeter-scale or larger solid particles (by radar, Blaauw 2017), up to 10s centimeters, as measured by lunar impact flushes (Yanagisawa et al. 2008, 2021; Szalay et al. 2018; Madiedo et al. 2019). The remarkable orbital feature is the small perihelion, $q = 0.14$ au, where Phaethon is repeatedly exposed to intense thermal processing at the peak sub-solar temperature $\gtrsim 1000$ K.

Spectroscopic measurements of sodium (Na) content of the Geminid meteors have been utilized for studying the thermal processes on Phaethon. The brightness of obtained spectra are at optical absolute magnitudes +4 or brighter, corresponding to meteoroid sizes $\gtrsim 1$ mm (e.g. Lindblad 1987). Sodium is relatively volatile metal element in meteoroids in most meteor showers, and commonly detected as neutral Na–D emission lines (NaI–doublet) at the wavelength $\lambda \sim 5890$ Å (Ceplecha et al. 1998). But, a notable feature of the Geminid meteors is that the extreme variety in their Na content, from depletion of the Na abundance ($\sim 7\%$ of the solar) (Kasuga et al. 2005) to near the solar-like values (e.g. Harvey 1973; Borovička 2001; Trigo-Rodríguez et al. 2003). Similar trends are reported from the measured intensity ratios of neutral metallic atom emission lines, as well as undetected NaI (Borovička 2001; Borovička et al. 2005, 2019). Kasuga et al. (2006) compiled Na in the Geminids in the last decade to investigate perihelion-dependent thermal effects on meteoroid streams. The effect is predicted to alter the metal abundances from their intrinsic values in their parents, especially for temperature-sensitive elements such as Na in alkaline silicates. However, as a result, the thermal desorption of Na is unlikely to occur for the Geminid stream even at $q = 0.14$ au. This is because the corresponding meteoroid temperature (characterized as large, compact, blackbody-like particle) does not reach the sublimation temperature of alkaline silicates (Kasuga et al. 2006)(also see, Springmann et al. 2019). The mm-scale or larger Geminid meteoroids take timescales of $\gtrsim 10^{4\sim 5}$ yr to lose Na (Čapek & Borovička 2009), being 1–2 orders of longer than the stream age $\tau_s \sim 1000$ (s)yr (Williams & Wu 1993; Ryabova 1999; Jakubík & Neslušan 2015) (Reviewed in Vaubaillon et al. 2019). Therefore the Na loss observed in the Geminid meteors must have originated from the thermal process of the parent, Phaethon (see a review, Kasuga & Jewitt 2019).

The parent body Phaethon has a diameter $D_e \approx 5\text{--}6$ km (Tedesco et al. 2004; Hanuš et al. 2016; Taylor et al. 2019; Dunham et al. 2019; Masiero et al. 2019; Devogèle et al. 2020)³ and an optically blue (B-type) reflection spectrum (e.g. Bus & Binzel 2002). While most images appear as a point source without any coma (Chamberlin et al. 1996; Hsieh & Jewitt 2005; Wiegert et al. 2008), recurrent dust-releasing activity has been optically observed only at the perihelion passage (Jewitt & Li 2010; Jewitt 2012; Jewitt et al. 2013; Li & Jewitt 2013; Hui & Li 2017). This is interpreted as a thermal-induced activity. The proposed mechanisms are thermal breakdown (Jewitt & Li 2010;

¹ GEM/4 from IAU Meteor Data Center, Nomenclature (Jopek & Jenniskens 2011)

² <https://ssd.jpl.nasa.gov/horizons/>

³ The effective spherical diameter $D_e \sim 5.5$ km (a mean equatorial diameter of 6.3 km) is estimated by the radar (Taylor et al. 2019) and $D_e = 5.2 \pm 0.1$ km is by the occultation (Dunham et al. 2019; Devogèle et al. 2020), respectively. These are the least model dependent.

Jewitt 2012), mass-shedding by thermal deformation (Nakano & Hirabayashi 2020), gas-dragged (or -gradient) force by sublimation of sodium (Masiero et al. 2021), and electrostatic repulsive forces (Jewitt 2012; Jewitt et al. 2015) which might be caused by accumulated sodium ions (Kimura et al. 2022). Constraints on mechanisms are provided both by the size of ejected particles and the mass-loss rates. The released particles are of micron size (measured from the short tail), too small compared to the millimeter~centimeter-sized Geminids. Such small particles would not be retained in the stream due to radiation pressure (Reviewed in Jewitt et al. 2015; Jewitt & Hsieh 2022). Larger particles (sizes $> 10\mu\text{m}$) must be in the Geminid stream (trail) as detected by the *DIRBE/COBE* thermal infrared survey from space (Arendt 2014). Furthermore, even if the measured perihelion mass-loss rates $\sim 3\text{kg s}^{-1}$ (Jewitt & Li 2010) sustained in steady-state over the entire orbit, it is orders of magnitude too small to supply the Geminid stream mass $M_s \approx 10^{13}\text{kg} - 10^{14}\text{kg}$ (Hughes & McBride 1989; Blaauw 2017) (cf. $\lesssim 10^{15}\text{kg}$ if cometary origin, Ryabova 2017) within its $\tau_s \sim 1000(\text{s})$ years of dynamical age. The observed particle size and mass-loss rate from Phaethon are not consistent with the Geminid stream, leading to the open question that how the stream was produced.

A non-negligible possibility is that the Geminids are the products of a catastrophic event (e.g. collision, disruption). Phaethon has a hypothetical breakup event which might occurred $> 10^4$ yr ago. This produced fragmental kilometer-sized NEAs: (155140) 2005 UD and (225416) 1999 YC (hereafter 2005 UD and 1999 YC, respectively), named as “Phaethon-Geminid Complex (PGC)” (Ohtsuka et al. 2006, 2008). The optical color of 2005 UD is blue (B-type), consistent with Phaethon (Jewitt & Hsieh 2006), but the dissimilarity in the concave-shaped near-infrared spectrum makes a direct association debatable (Kareta et al. 2021; MacLennan et al. 2022). The color of 1999 YC in the visual band distinctly exhibits a neutral (C-type) slope (Kasuga & Jewitt 2008). The PGC-asteroids show some physical similarity, but their dynamical association is unclear (see a review, Kasuga & Jewitt 2019). Relevantly, Phaeton is proposed to have its precursor origin in the main-belt. The dynamical lifetime of 26 Myr can be linked back to (2) Pallas (de León et al. 2010) with $\sim 2\%$ chance (Todorović 2018) or to the inner main-belt asteroids (e.g. (329) Svea or (142) Polana) with $\sim 18\%$ chance (MacLennan et al. 2021). The links are of very low probabilities and still unsure, but imply that Phaeton itself could be a disrupted fragment from one of these sources. To summarize, the Geminid stream and Phaethon, both are likely to be formed stochastically rather than in steady-state, however the nature of the events are not clarified yet.

In this paper we present a space-based thermal infrared study of the Geminid-related NEAs: Phaethon, 2005 UD and 1999 YC using the NASA spacecraft *Wide-field Infrared Survey Explorer* (WISE; Wright et al. 2010) and the successive project *Near-Earth Object WISE* (NEOWISE; Mainzer et al. 2011, 2014). Long wavelength observations are aimed at larger particles potentially containing much more mass. The multiple observing epochs contain data from four infrared wavelength bands: $3.4\mu\text{m}$ (*W1*), $4.6\mu\text{m}$ (*W2*), $12\mu\text{m}$ (*W3*), and $22\mu\text{m}$ (*W4*), providing opportunities to constrain the dust environments around Phaethon, 2005 UD and 1999 YC over the last decade. The each band is specified for investigating different physical characters of the PGC-asteroids, such as the dust production rate (*W1*), the gas production rate (*W2*) and dust trails and potentially co-moving objects (*W3* and *W4*). Another motivation is to find an activity mechanism far from perihelion, which is different from thermal-related production. This study provides a groundwork for JAXA’s *DESTINY+* mission which is planning to flyby at the distance of 500 km from Phaethon in 2028, with a potential extended mission to flyby 2005 UD (Ozaki et al. 2022).

2. WISE/NEOWISE DATA

The near- and mid-infrared data were taken by *WISE* (Wright et al. 2010) and NEOWISE (Mainzer et al. 2011, 2014). *WISE* is equipped with a 40 cm diameter telescope, which was launched on 2009 December 14 into a Sun-synchronous polar orbit. The full sky survey was conducted using four infrared wavelength bands centered at $3.4\mu\text{m}$ (*W1*), $4.6\mu\text{m}$ (*W2*), $12\mu\text{m}$ (*W3*), and $22\mu\text{m}$ (*W4*). It was continued until 2010 September 29 when the cryogen was exhausted. Then *WISE* further continued surveying in a post-cryogenic two-band survey mode until 2011 February 1 when it was put into hibernation. On 2013 December 13, NEOWISE resumed the two-band survey (*W1* and *W2*), which is currently ongoing as a reactivation mission (NEOWISE-R).

The spacecraft employs two-types of focal plane array detectors, the HgCdTe (Teledyne Imaging Sensors) in the shorter wavelength bands (*W1* and *W2*) and the Si:As BIB (DRS Sensors & Targeting Systems) in the longer wavelength bands (*W3* and *W4*) (Wright et al. 2010). Both detectors have 1024×1024 pixels, each $2''.76 \text{ pix}^{-1}$ in the *W1*, *W2* and *W3* bands and $5''.5 \text{ pix}^{-1}$ (2×2 binned) in the *W4* band. The corresponding field of view (FOV) is $47' \times 47'$. With the dichroic beam splitters, consecutive frames were simultaneously imaged through the same FOV in each band every 11 second. The exposure time was 7.7 seconds in the *W1* and *W2* bands and 8.8 seconds in the *W3* and *W4* bands, respectively (Wright et al. 2010). The data of *WISE* (*W1*–*W4*) and NEOWISE (*W1* and *W2*) are available at the NASA/IPAC Infrared Science Archive (IRSA⁴). The instrumental, photometric, and astrometric calibrations are detailed in Cutri et al. (2012, 2015).

We used the IRSA search tools (GATOR⁵ and WISE Image Service⁶) to retrieve all detections of the three PGC asteroids: Phaethon, 2005 UD and 1999 YC. In the GATOR, the queried sources are WISE All-Sky Single Exposure (L1b) (WISE Team 2020a), WISE 3-Band Cryo Single Exposure (L1b) (WISE Team 2020b), WISE Post-Cryo Single Exposure (L1b) (WISE Team 2020c), and NEOWISE-R Single Exposure (L1b) (NEOWISE Team 2020). The detections were double-checked with the WISE Image Service, and compared with the list from the Minor Planet Center (MPC) database⁷. Here, we applied the screening process to the data described in Masiero et al. (2011); Hung et al. (2022). We based our selection criteria on high Signal-to-Noise Ratio (SNR) (> 5) in at least one band, moon angular separation > 30 degrees, and angular distance from the nominal boundaries of the South Atlantic Anomaly (SAA) $\gtrsim 10$ degrees. We selected observations having flags of `cc_flags` = 0 which secures no contamination produced by known artifacts, e.g. latent images or diffraction spikes (Mainzer et al. 2011). We used the profile-fit photometric quality flag of `ph_qual` = A, B, C or U which corresponds to $\text{SNR} \geq 10$, $3 < \text{SNR} < 10$, $2 < \text{SNR} < 3$ and $\text{SNR} \leq 2$ ($= 2\sigma$ upper limit on magnitude, see also § 3.1), respectively. The highest frame quality score of `qual_frame`=10 is used.

The *WISE*/NEOWISE data reduction pipeline conducts initial nonlinearity and saturation correction for data brighter than the threshold of *W1* = 8.1 mag, *W2* = 6.7 mag, *W3* = 3.8 mag, and *W4* = -0.4 mag, however further analysis shows that additional corrections are needed (Cutri et al. 2012, 2015)⁸. For Phaethon taken on MJD 58104.2148 (UT 2017-Dec-17), the measured magnitudes listed in the catalog, *W1*= 7.745 ± 0.014 mag and *W2*= 2.894 ± 0.003 mag, are in the saturated regime. We

⁴ <https://irsa.ipac.caltech.edu/frontpage/>

⁵ <https://irsa.ipac.caltech.edu/cgi-bin/Gator/nph-scan?submit=Select&projshort=WISE>

⁶ <https://irsa.ipac.caltech.edu/applications/wise/>

⁷ https://minorplanetcenter.net/db_search

⁸ https://wise2.ipac.caltech.edu/docs/release/allsky/expsup/sec6_3d.html

corrected their saturation biases using the relations derived for those of specific catalog magnitudes⁹ (cf. Masiero et al. 2019),

$$\begin{aligned} W1(\text{out}) &= W1(\text{in}) + (0.037 \pm 0.039) \text{ mag}, \\ W2(\text{out}) &= W2(\text{in}) + (1.330 \pm 0.221) \text{ mag}. \end{aligned} \tag{1}$$

We substitute $W1(\text{in})=7.745\pm 0.014$ mag and $W2(\text{in})=2.894\pm 0.003$ mag into Equation (1), and we obtain the corrected magnitude $W1(\text{out})=7.782\pm 0.041$ mag and $W2(\text{out})=4.224\pm 0.221$ mag, respectively.

We visually checked the image data to remove star contamination that might appear in the shorter bands ($W1$ and $W2$) even if they do not appear in the longer wavelength bands ($W3$ and $W4$). This is because the stellar thermal signatures ($\gtrsim 2000$ K) have their blackbody peaks in the shorter wavelengths and have flat decreasing spectra, representing $W1$ SNR $>$ $W2$ SNR. Likewise, as for the two-band detections of NEOWISE, we removed the contamination by requiring $W1 - W2 > 1$ mag. The principle is more detailed in Masiero et al. (2018, 2020). We actually find this issue in 1999 YC taken by *WISE* on MJD 55213.7089 (UT 2010-Jan-17), requiring us to drop its shorter bands. Finally we again visually conducted spot check on all of the selected data to ensure no corruptions in the images. The image corrupted by artifacts and noises are avoided. We found five observation epochs for Phaethon, three for 2005 UD and two for 1999 YC. The observation log is shown in Table 1. The orbital information is summarized in Table 2.

Next, we inspected the full-width half maximum (FWHM) of asteroid images to find if the surface brightness profiles can be used to set their activity limits (Jewitt et al. 2019). We here show an example of Phaethon’s point-spread function (PSF) taken in the $W3$ band on MJD 55203.2564 (UT 2010-Jan-07). The FWHM of Phaethon is $\theta_F=7''.8$, beyond the diffraction limit of the *WISE* instrument $\theta_d=6''.4$ ($=1.03 \lambda/D$ in radians, where $\lambda=12\mu\text{m}$ is the wavelength band center and $D=40$ cm is the telescope diameter). For comparison, the FWHM of nearby field stars is $\sim 6''.6$ (medium value of seven field stars). The angular diameter of Phaethon (a diameter $D_e \sim 5$ km at $\Delta \sim 2.08$ au) subtends $\theta_{Ph}=0''.0031$, which is negligibly small. The derived composite width of Gaussian is $6''.4$ ($= (\theta_d^2 + \theta_{Ph}^2)^{0.5}$), which is not sufficient to resolve the Phaethon image. The same circumstance is found for the other data of interest. Therefore, the surface brightness profiles are not expected to give useful limits to their activity levels.

In this study, we use the effective spherical diameters (D_e) and geometric visible albedos (p_v) determined from *WISE*/NEOWISE (Table 3). Many observing-epochs cover multiple viewing geometries, producing the refined data sets in the uniformity and calibration. Phaethon, for example, five epochs of data estimated $D_e=4.6_{-0.3}^{+0.2}$ km by applying Thermophysical model (TPM) fits (Masiero et al. 2019). The accuracy is validated by comparing the estimated sizes of 23 main-belt asteroids (surface temperature variation is stable) from NEOWISE with those from occultation/spacecraft as the ground-truth sizes (Masiero et al. 2019). The size is consistent within 2σ of the other TPM result $D_e=5.1\pm 0.2$ km (Hanus et al. 2016, 2018), while not consistent with $D_e\sim 5.5$ km showing a muffin-top shape (equatorial bulge of 6.3 km) as observed by Arecibo radar during the apparition in 2017-Dec (Taylor et al. 2019). The shape model or observed orbital positions (pre- or post- q) may require some offsets in size estimations and thermophysical behavior (MacLennan & Emery 2021; MacLennan et al. 2022).

⁹ https://wise2.ipac.caltech.edu/docs/release/neowise/expsup/sec2_1civa.html

Here, we describe the justification for applying the *WISE*/NEOWISE-derived size with its spherical assumption. The thermal survey and radar data have a huge difference in the resolution, for example 140 km pix^{-1} (NEOWISE) vs. $0.075 \text{ km pix}^{-1}$ (Arecibo) at the Phaethon’s closest distance ($\Delta=0.069 \text{ au}$). The infrared data do not resolve a 5-6 km asteroidal shape, indicating that the assumption of spherical body is reasonable for the usage of *WISE*/NEOWISE alone. The post- q data tend to estimate larger sizes than those of pre- q data due to significant bias suffered from extreme heating at its perihelion passage (MacLennan et al. 2022). In such a case, the pre- q data use a stable variation of surface temperature presumed to be plausible for obtaining the statistically best-fitted size $D_e=4.8\pm 0.2 \text{ km}$ (Table 4 in MacLennan et al. 2022). This is consistent within 1σ of our *WISE*/NEOWISE-derived size. On the other hand, the km-scale asteroids with a few epochs of data find that the TPM-fitted size is consistent within $\lesssim 0.1 \text{ km}$ of the other model (Masiero et al. 2019). Thus we apply the unified uncertainty in Phaethon size, i.e. $D_e=4.6\pm 0.3 \text{ km}$ for simplicity of use.

3. ANALYSIS

3.1. Photometry, Calibration and Conversion from Magnitude to Flux Density

The photometry and calibration methodology are given by the IRSA website¹⁰ (Cutri et al. 2012, 2015). Magnitudes are measured based on the median FWHM of the PSF of the asteroid at the each band. The aperture radius is set as $1.25 \times \text{FWHM}$, where the FWHM adopts $6''$, $6''$, $6''$, and $12''$ in bands W1 through W4, respectively¹¹. When the Profile-fitting Photometry (WPRO) or Aperture Photometry System (WAPP) measure the flux with the $\text{SNR} \leq 2$, magnitude uncertainty is expressed as “NULL” and the calibrated magnitude is interpreted as the 2σ upper limit¹². Those results are listed without uncertainties in Table 1.

The measured magnitudes are converted into the flux density (Jy) using the published zero points and the color corrections (Wright et al. 2010). The derived flux density can be converted to SI units ($\text{W m}^{-2} \mu\text{m}^{-1}$) using the relative system response curves (RSRs) and the zero magnitude attributes (Table 1, Jarrett et al. 2011). The measured instrumental source brightness (in digital numbers) is calibrated by referring an instrumental zero point magnitude¹³ (Cutri et al. 2012, 2015). Hereafter we apply the procedure as appropriate.

3.2. Reflected Sunlight Removal

The asteroids from *WISE*/NEOWISE comprise a blend of reflected sunlight and thermal emission. It is significant in the shorter bands (*W1* and *W2*) of km-sized NEAs (Mainzer et al. 2011; Nugent et al. 2015). Here we remove the reflected sunlight to extract thermal emission alone.

The flux density of reflected sunlight from an asteroid, F_ν^{Ref} (Jy), is calculated correcting the Sun-observer-object distance for each frame, using the equation

$$F_\nu^{\text{Ref}} = \frac{\pi B_\nu(T_\odot) R_\odot^2}{R_h^2} A \pi \left(\frac{D_e}{2}\right)^2 \frac{\Phi_{\text{vis}}(\alpha)}{\Delta^2}, \quad (2)$$

where B_ν is the Planck function (Jy sr^{-1}) at the Solar temperature $T_\odot = 5778 \text{ K}$, $R_\odot = 6.957 \times 10^{10} \text{ cm}$ is the Solar radius, R_h is heliocentric distance (cm). The $A \approx A_v = q p_v$ is the bolometric Bond albedo

¹⁰ <https://wise2.ipac.caltech.edu/docs/release/allsky/expsup/sec4.4h.html>

¹¹ <https://wise2.ipac.caltech.edu/docs/release/allsky/expsup/sec4.4c.html>

¹² <https://wise2.ipac.caltech.edu/docs/release/allsky/expsup/sec4.4c.html#ul2>

¹³ <https://wise2.ipac.caltech.edu/docs/release/allsky/expsup/sec4.4h.html#CalibratedM>

(scattered fraction of the incident solar flux), where q is the phase integral (measure of the angular dependence of the scattered emission), and p_v is the visible geometric albedo. Based on the shape of phase curve in the $H - G$ model of [Bowell et al. \(1989\)](#), we adopt $q=0.3926$ from $q=0.29+0.684G$ where $G=0.15$ is the phase slope parameter. D_e is the asteroid diameter (cm), $\Phi_{\text{vis}}(\alpha)$ is the phase function (Equation (A4) of [Bowell et al. 1989](#)) in which α is the phase angle (in degrees), and Δ is the *WISE*-centric distance (cm). Using the measured values of D_e and p_v from *WISE/NEOWISE* (Table 3), we obtained F_ν^{Ref} to remove from the measured flux. The extracted thermal flux density is summarized in Table 4.

3.3. Temperature

In order to estimate an effective temperature, T_{eff} (K), we use the thermal flux densities at the $W3$ ($12\ \mu\text{m}$) and $W4$ ($22\ \mu\text{m}$) from *WISE*. The shorter wavelength bands ($W1$ and $W2$) are avoided to prevent any contamination from remaining blended sources. The ratio of flux density, $W3/W4$, corresponds to the ratio calculated from a blackbody having T_{eff} ([Jewitt et al. 2019](#)). As a reference, an equilibrium blackbody temperature (T_{bb}) of a sphere, isothermal object at the same heliocentric distance (R_h) is given. The results are shown in Table 5.

The derived effective temperature is close to blackbody temperature, $T_{\text{eff}} \approx 0.98 \times T_{\text{bb}}$. This suggests that Phaethon and 1999 YC are approximately considered as sphere, blackbody-like objects in the *WISE/NEOWISE* data. This interpretation is different from the previous high-resolved thermal image of Phaethon. During its 2017 flyby, the *VLT* obtained the excess effective temperature ($T_{\text{eff}} \approx 1.14 \times T_{\text{bb}}$), implying that Phaethon ($D_e \sim 5\ \text{km}$) has a non-spherical, non-blackbody features in detail ([Jewitt et al. 2019](#)). The difference in T_{eff} could be caused by the difference in the observed phase angle. While *WISE* observed Phaethon at $\alpha=25^\circ$ (Table 1), the *VLT* was at $\alpha=66^\circ$ ([Jewitt et al. 2019](#)). The latter would see both the hot dayside and the cold nightside. For NEAs, the night-side flux could be important at high phase angle ([Harris 1998](#); [Mommert et al. 2018](#)), although this interpretation comes from classical thermal models with uncertain parameters (e.g. a beaming parameter: η , see § 3.4). Regarding this, 2005 UD (MJD 58383: 2018-Sep-22) and 1999 YC (MDJ 57739: 2016-Dec16) taken at $\alpha > 75^\circ$ by NEOWISE (Table 1) would also include their night-side fluxes in the measurement. However our method is independent of those of models and the *WISE/NEOWISE* resolution is limited. Thus we assume 2005 UD and other NEOWISE data also have a blackbody-like temperature (Table 5).

3.4. Thermal Flux Density

The thermal flux density from an asteroid, F_ν (Jy), is calculated using Equation (1) of [Mainzer et al. \(2011\)](#),

$$F_\nu = \epsilon \left(\frac{D_e}{2} \right)^2 \frac{1}{\Delta^2} \int_0^{\pi/2} \int_0^{2\pi} B_\nu(T(\theta, \phi)) d\phi \sin \theta \cos \theta d\theta, \quad (3)$$

where $\epsilon = 0.9$ is the infrared emissivity for the typical value of silicate powders from laboratory measurements ([Hovis & Callahan 1966](#); [Lebofsky et al. 1986](#)), $B_\nu(T(\theta, \phi))$ is the Planck function (Jy sr⁻¹) for the surface temperature $T(\theta, \phi)$ (K) in which θ (in degrees) is the angle from the sub-observer point to a point on the asteroid such that θ is equal to the phase angle α (in degrees) at the sub-solar point, and ϕ (in degrees) is an angle from the sub-observer point such that $\phi = 0$ at the sub-solar point ([Mainzer et al. 2011](#)). We again adopt the same values of D_e (cm) and Δ (cm)

in section 3.2 (Tables 1 and 3). The surface temperature, $T(\theta, \phi)$, is calculated using Equation (2) of Mainzer et al. (2011),

$$T(\theta, \phi) = T_{\text{ss}}[\max(0, \cos \theta \cos \alpha + \sin \theta \sin \alpha \cos \phi)]^{\frac{1}{4}}, \quad (4)$$

where T_{ss} is the sub-solar temperature (K) derived by $T_{\text{ss}} = \chi^{\frac{1}{4}} \cdot T_{\text{eff}}$ (Jewitt & Luu 1992). The nondimensional parameter χ ($1 \leq \chi \leq 4$) represents the surface area ratio of the absorbing surface to the surface that is emitting the absorbed heat energy (Jewitt & Kalas 1998). For instance, $\chi=1$ for a subsolar patch on a non-rotating asteroid and $\chi=4$ for a spherical, isothermal asteroid in which the Sun's heat is absorbed on πr^2 and radiated from $4\pi r^2$ (Li & Jewitt 2015). We adopt $\chi = 2$ corresponding to thermal radiation from an asteroid hemisphere (observable-side). As examples, calculated spectral energy distributions and observed flux densities of Phaethon (MJD 55203.2564: 2010-Jan-07), 2005 UD (MJD 58383.2977: 2018-Sep-22), and 1999 YC (MJD 55213.6428: 2010-Jan-10) is shown in Figure 1, 2, and 3, respectively.

We have a short note on the assumption of zero night-side emission. The classical thermal models generally use the nonphysical beaming parameter (η) for the sub-solar temperature (T_{ss}) to adjust the angular temperature distribution (anisotropy) of the thermal emission, as seen in the Standard Thermal Model (STM), Fast Rotating Model (FRM) (Reviewed in Lebofsky & Spencer 1989) and the near-Earth asteroid thermal model (NEATM) (Harris 1998). The common issue in those of models is that the strong dependence on η which is not an intrinsic property for the temperature distribution over the observable surface of asteroid. Also it varies with observing geometry (α , R_{h} and Δ), as well as the physical properties (e.g. thermal inertia) of the asteroid (See §3.4, Wright et al. 2018) (See also Masiero et al. 2019). Thus we avoid the ambiguity of η .

4. RESULTS

Our images of Phaethon, 2005 UD and 1999 YC each look like point sources and show no apparent evidence of coma activity. When both the reflected sunlight and thermal emission from the asteroids are removed (§ 3.2 and 3.4), residuals remain in some data. For active comets, the excess signals in the $W1$ and $W2$ bands of *WISE*/*NEOWISE* can be used to estimate the dust and gas (CO and CO₂) production rates respectively (Bauer et al. 2008, 2011, 2015, 2021; Mainzer et al. 2014). The longer wavelength bands ($W3$ and $W4$) are capable of examining the dust trails and potentially detect co-moving objects (cf. Reach et al. 2000, 2007; Jewitt et al. 2019). Here, we assess the significance of the excess signals and attempt to set an empirical upper limit to the production rates, dust trails and co-moving objects.

4.1. Dust Production Rate: $W1$

We look into the dust production rate with the $W1$ ($3.4 \mu\text{m}$) data following the methodology in Bauer et al. (2008, 2011, 2021). The reflected dust signal is typically considered to dominate in the band for all but the nearest NEOs. Even when comets sublimate their abundant icy volatiles, dust comprise $\gtrsim 70\%$ of the total signal (Bockelée-Morvan et al. 1995; Reach et al. 2013) (Summarized in Bauer et al. 2015). Assuming the excess flux density is produced by coma brightness, the mass of dust particles scattering in the coma, M_d (kg), is given by (Equations (3) and (5) of Bauer et al. 2008)

$$M_d = \frac{a_d \rho_d}{3} \times \pi D_e^2 \frac{F_{\text{total}} - F_{\text{calc}}}{F_{\text{calc}}}, \quad (5)$$

where $a_d = 1.7 \mu\text{m}$ (1/2 of the *W1* wavelength, [Bauer et al. 2011](#)) is the radius of the dust particle contributing to coma brightness, $\rho_d = 2000 \text{ kg m}^{-3}$ is the assumed common bulk density of dust and asteroid (cf. Phaethon, [Hanuš et al. 2018](#)), D_e (m) is the diameter of the asteroid, F_{total} (Jy) is the measured total flux density from an asteroid, and F_{calc} (Jy) is the calculated flux density from an asteroid (= reflected sunlight + thermal emission). The dust production rate, Q_{dust} (kg s^{-1}), is estimated using M_d (kg), velocity of dust, v_d (km s^{-1}), and projected size of the dust coma, R_d (km) ($\approx \rho$ in the *Af ρ* method, [A’Hearn et al. 1984](#)). The traveling time for the produced dust from the asteroid is t_d (second) = R_d/v_d , and using the Equation (6) of [Bauer et al. \(2008\)](#), we obtain the relation

$$Q_{\text{dust}} = \frac{M_d}{t_d} = \frac{M_d}{R_d} v_d, \quad (6)$$

where R_d (km) is the size of subtended area using an aperture radius of the of $7''.5$ at the *WISE*-centric distance Δ (au), and v_d is adopted as the escape velocity from the PGC asteroids, i.e. $v_d \sim 3 \text{ m s}^{-1}$ for Phaethon and $v_d \sim 1 \text{ m s}^{-1}$ for 2005 UD and 1999 YC, respectively. The obtained mass loss rates are shown in Table 6.

We find no strong variation in the production rate at different epochs, and find no dependency on the location of the object in the orbit at the time of observation. The upper limit to the mass-loss rate for Phaethon is $Q_{\text{dust}} \lesssim 2 \text{ kg s}^{-1}$ and those of 2005 UD and 1999 YC are both $Q_{\text{dust}} \lesssim 0.1 \text{ kg s}^{-1}$, respectively. The *WISE*/NEOWISE-derived rate limits are 1–2 orders of magnitude larger than those of optically measured limits at the R_c -band of $0.001 - 0.01 \text{ kg s}^{-1}$ ([Hsieh & Jewitt 2005](#); [Jewitt & Hsieh 2006](#); [Kasuga & Jewitt 2008](#)). Meanwhile, our Q_{dust} is ~ 10 times lower than the limit of $\lesssim 14 \text{ kg s}^{-1}$ measured at the mid-infrared band ($\lambda=10.7 \mu\text{m}$) from Phaethon ([Jewitt et al. 2019](#)).

The estimated limiting mass-loss rates of Phaethon can be compared with the total mass of the Geminid meteoroid stream. The Geminid stream mass, $M_s \approx 10^{13} \text{ kg} - 10^{14} \text{ kg}$ ([Blaauw 2017](#)) is thought to have been produced from Phaethon over the last $\tau_s \sim 1000(s)$ years (e.g. [Williams & Wu 1993](#)). The steady-state mass-loss rate needed, $dM_s/dt \sim M_s/\tau_s \sim 320 - 3200 \text{ kg s}^{-1}$, is comparable to those of active Jupiter family comets (JFC). This requires at least 10–100 times larger rates than the observed rates in the near- and mid-infrared bands ($3.4 \mu\text{m}$ and $10.7 \mu\text{m}$). The leading conclusion is that the production of the Geminids occurred episodically, such as catastrophic breakup of a precursor body, not in steady disintegration at the observed rates (cf. [Jewitt et al. 2019](#)). Likewise, to estimate the mass-loss rate (Q_{dust}) from 2005 UD, we estimate the mass of the Daytime Sextantid meteoroid stream. The stream age is calculated to be $>10^4$ yr ([Jakubík & Neslušan 2015](#)), comparable to the last lowest perihelion-passage ($\approx 2 \times 10^4$ yr ago, [MacLennan et al. 2021](#)). Assuming that the meteoroids have been released from 2005 UD over the age of 10,000 yr, the maximum mass-loss rate $Q_{\text{dust}} \lesssim 0.1 \text{ kg s}^{-1}$ finds the total mass of the Daytime Sextantid stream $\sim 10^{10} \text{ kg}$. Note that if 2005 UD shared a precursor body with Phaethon, the resulting breakup event could provide more mass in the stream. To investigate the possibility of a breakup-induced stream formation, longer wavelength observations of the parental asteroids to detect larger particles, potentially containing much more mass, are worthwhile to continue ([Jewitt et al. 2015](#); [Kasuga & Jewitt 2019](#)). Further observations of the Geminids and the Daytime Sextantids and connection to a stream model will be helpful to understand the stream formation processes.

4.2. Gas (CO and CO₂) Production Rate: W2

Active comets showing excess flux density in the $W2$ ($4.6\mu\text{m}$)-band is attributable to gas emission lines, in particular the CO_2 ν_3 vibrational fundamental band ($4.26\mu\text{m}$) and the CO $v(1-0)$ rovibrational fundamental bands ($4.67\mu\text{m}$) (Pittichová et al. 2008; Ootsubo et al. 2012; Bauer et al. 2011, 2015, 2021; Rosser et al. 2018). These volatiles have low sublimation temperatures of 20–100 K, presumed to be preserved in frozen ices or trapped as gases in the nuclei (Prialnik et al. 2004; Bouziani & Jewitt 2022).

This gas emission is unlikely to be present in the case of the PGC-asteroids because of their thermophysical and dynamical properties (Jewitt et al. 2018, 2019). The surface temperatures at perihelia are $T_{\text{ss}}^{\text{PGC}} \gtrsim 800$ K, too hot for ice to survive. The largest plausible thermal diffusivity $\kappa \sim 10^{-6} \text{ m}^2 \text{ s}^{-1}$ is appropriate for rock (a compact dielectric solid). The diurnal thermal skin depth, d_s , is estimated by $\sim \sqrt{\kappa P_{\text{rot}}}$, where P_{rot} is the rotational period. Setting $\kappa = 10^{-6} \text{ m}^2 \text{ s}^{-1}$ and $P_{\text{rot}} = 3.6 - 5.2$ hr for the PGC asteroids (Table 2, Kasuga & Jewitt 2019) find $d_s \sim 0.14$ m at deepest. The q -temperature at the thermal skin depth is > 200 K ($= T_{\text{bb}}^{\text{PGC}}/e$), far above the sublimation temperature of CO_2 and CO . The heat conduction timescale corresponding to the equator radius of Phaethon ($r \sim 3$ km) is 0.3 Myr ($\approx r^2/\kappa$), about two orders of magnitude shorter than its dynamical lifetime of 26 Myr (de León et al. 2010). The core temperatures of the PGC asteroids are sufficiently heated at $T_{\text{core}} \gtrsim 280$ K (Equation (4) of Jewitt & Hsieh 2006). Dynamical simulations find that Phaethon on its present orbit could lose all internal ice (e.g. H_2O) over a very short timescale of 5–6 Myr (Yu et al. 2019; MacLennan et al. 2021). Therefore, the PGC-asteroids are highly unlikely to be reservoirs for the icy species (CO_2 and CO) which are not expected to survive on the surfaces or in the interiors. We thus do not make further discussion on this topic.

4.3. Dust Trail: $W3$ and $W4$

We search for dust trails that presumably formed from the mass-loss of the PGC-asteroids. Such trails consist of larger, slow-moving dust particles that would be insensitive to solar radiation pressure. These particles would follow the parent bodies’ heliocentric orbits and stay close to those orbital planes (Reviewed in Jewitt et al. 2015). Previous thermal observations (*DIRBE/COBE*) managed to detect the surface brightness of the Phaethon’s dust trail, consisting of larger particles with sizes $>10 \mu\text{m}$ (Arendt 2014). For all of the small bodies observed by *WISE/NEOWISE*, the both $W3$ - and $W4$ -bands are dominated by thermal emission (Mainzer et al. 2011). Since the PGC-asteroids have blackbody-like temperatures (Table 5), the Wien’s displacement law ($\lambda_{\text{max}} \cdot T_{\text{eff}} = 2898 \mu\text{m K}$ gives $\lambda_{\text{max}}=10.7\sim 15.8\mu\text{m}$) indicates that the $W3$ -band ($12\mu\text{m}$) is the most effective wavelength for larger particles. Thus we primarily study the $W3$ -data of Phaethon and 1999 YC, and the $W4$ -data is supplementary compared. Unfortunately *WISE* did not observe 2005 UD during the cryogenic mission, so we do not have $W3$ or $W4$ data for this object.

During the survey, the apparent motion of the asteroids with respect to the *WISE* location had rates up to approximately $28'' \text{ hr}^{-1}$ in right ascension (RA) and $-32'' \text{ hr}^{-1}$ in declination (DEC)¹⁴. The corresponding drift across the frame is $\lesssim 0.1''$ during each exposure. These rates are more than an order of magnitude smaller than the pixel scale ($2''.76 \text{ pix}^{-1}$), meaning that smearing within an image is negligibly small. For this analysis, we do not include data in which asteroid is taken close to edge of the frame, where trail location is expected to be out of FOV. Also we avoid images in which trail’s expected direction is contaminated by stars. Detectability of a trail is improved for

¹⁴ NASA JPL HORIZONS <https://ssd.jpl.nasa.gov/horizons/>

small out-of-plane angles, δ_{\oplus} , which is given by the angle between the observer and target orbital planes (Jewitt et al. 2018). The $\delta_{\oplus}=3.8^{\circ}$ for Phaethon indicates it should be highly sensitivity to the dust trail close to the plane, while $\delta_{\oplus}=-23^{\circ}$ for 1999 YC is slightly worse.

The *W3* image was corrected by subtracting a bias constructed from a median-combination of applied images (Table 1). The orientation of each image was rotated to bring the direction of the position angle (PA) of north to the top and east to the left, and shifted to align the images using fifth-order polynomial interpolation. The images were then combined into a single summed image. The resulting summed image of Phaethon has a FWHM of $7''.8$, and is shown in Figure (4). Likewise, the summed image of 1999 YC with a FWHM of $7''.1$ is shown in Figure (5). No asteroid-associated dust trails, which are expected to be parallel to the “ $-V$ ” vector, are apparent in either Figure.

In general, highly-resolved observations of asteroidal dust trails have clarified their morphological properties. For example, the trail widths of active main-belt asteroids are commonly very narrow, near the bodies, and represent rather recently ejected debris. The FWHM of trail widths of 300–600 km ($< 1''$) are typically very narrow, as measured from 133P/Elst-Pizarro and 311P/PanSTARRS (P/2013 P5) (§3.1, Jewitt et al. 2018). Small ejection velocities of $\sim 1\text{--}2\text{ m s}^{-1}$ in the perpendicular direction to the orbital plane, comparable to the gravitational escape speed (V_{esc}), are measured for most active asteroids (Jewitt et al. 2015).

However, this expectation is unlikely to hold for Phaethon. The width of the Phaethon dust trail (Geminid stream) is expected to be wider than those of asteroidal trails. Optical observations of the Geminid meteor shower estimate the shower duration time. The shape of zenithal hourly rate (ZHR) of the Geminids is asymmetric at the peak time with its minimum FWHM of $\gtrsim 1^{\circ}$ in the solar longitude, corresponding to the duration time $\gtrsim 24\text{ hr}$ (Uchiyama 2010). Geometrically, the Earth ($v_{\oplus}=30\text{ km s}^{-1}$) cuts through the stream at the crossing angle of 62° on the projected ecliptic plane (Mikiya Sato, private communication). Thus we find the Geminid stream width has a FWHM $\sim 2.3\times 10^6\text{ km}$ ($= 30\text{ km s}^{-1} \times 24\text{ hr} \times 3600\text{ s hr}^{-1} \times \sin(62^{\circ})$). For 1999 YC, neither its activity nor trail has been observed yet (Kasuga & Jewitt 2008). Assuming that 1999 YC had a trail, and the width FWHM would be at most $V_{\text{esc}}\cdot P_{\text{orb}}/4$, where P_{orb} is the orbital period and 4 is because a particle nearly spends 1/4 orbit rising from the orbital plane to the peak height (David Jewitt, private communication). Substituting $V_{\text{esc}}\sim 1\text{ m s}^{-1}$ and $P_{\text{orb}}=1.7\text{ yr}$, the trail width FWHM would be expected to be about $1.3\times 10^4\text{ km}$. Such a trail could be imaged by *WISE*, if it existed and was bright enough, as the *WISE* images have a resolution of $2,400\text{ km pix}^{-1}$ at the observed $\Delta=1.22\text{ au}$ to 1999 YC.

To measure surface brightness profiles perpendicular to the expected trail direction (“ $-V$ ”), the summed images of Phaethon and 1999 YC were each rotated to set the projected orbit direction to the horizontal. Both the *W3* and *W4* images are used for comparison. We average $\pm 1\text{ pix}$ ($2''.76$ for *W3* or $5''.5$ for *W4*) left and right of the object at a distance of $50\text{--}215''$ from the asteroids. The profile for Phaethon and 1999 YC is shown in Figure (6) and (7), respectively. The green region corresponds to approximate width of trail. For Phaethon (Figure 6), a trail would be detected as a symmetric excess at $x = 0''$ and $\sim 1530''$ wide if FWHM $\sim 2.3\times 10^6\text{ km}$. Likewise for 1999 YC (Figure 7), the calculated trail width FWHM $\sim 1.3\times 10^4\text{ km}$ has a symmetric green region centered at $x = 0''$ and $\sim 16''$ wide. No excess is evident in the profiles shown, neither in the *W3*-band nor in the *W4*-band measured at distinctive distance combinations of vertical cuts. We find no any hint of an orbit-aligned trail, or any thickness.

Here, we have a short note on the non-detection of the Phathon trail by *WISE*. This result is contrary to *DIRBE/COBE*, probably caused by observing geometry. *WISE* measured Phaethon and its vicinity at the solar elongation $\varepsilon \sim 91^\circ$ and $R=2.32$ au. On the other hand, *DIRBE/COBE* detected the surface brightness of the trail at $\varepsilon \sim 64^\circ$ and $R=1.01$ au (Arendt 2014), when it was much closer to the sun, so much warmer and less dispersed. *WISE* was at a rather disadvantageous observing point for trail thermal emission. Despite this, the background in the *WISE* images can set a uniformly applicable limit for constraining signals referring the morphological evidence from the asteroids.

We set a practical upper limit to the surface brightness of the potential dust trails. The *W3*-band ($12\mu\text{m}$) is inspected because of the most efficient SNR. We sampled 70 pix ($193''$) along the trail direction from the each asteroid. The profile was averaged along the rows over the width FWHM of the trail. Two-consecutive highest counts were selected and averaged between the distances for placing a statistical limit. For the Phaethon trail, we used the angular distances $33'' \leq \theta_{\text{od}} \leq 36''$ which corresponds to the distances of $5.0 \sim 5.4 \times 10^4$ km from Phaethon. For the 1999 YC trail, we used the angular distances of $69'' \leq \theta_{\text{od}} \leq 72''$ which corresponds to the distances of $6.1 \sim 6.4 \times 10^4$ km from 1999 YC. The measured counts (in digital numbers) were converted to the flux density (in Jy, see § 3.1). The ratio of the measured flux density scattered by the dust particles in the trail I_d (Jy) to the measured flux density scattered by the asteroid (nucleus) cross section I_n (Jy), which corresponds to the ratio of the dust cross section in the trail C_d (km^2) to the asteroid (nucleus) cross section C_n (km^2), can be calculated (Luu & Jewitt 1992), and is expressed as

$$\frac{I_d}{I_n} = \frac{C_d}{C_n}. \quad (7)$$

The optical depth was obtained from $\tau = C_d/s^2$, where $s(\text{km})=725.27 \cdot \Delta$ is the linear distance (corresponding to 1 arcsecond) at the *WISE*-centric distance Δ (in au) of the asteroid. The results are summarized in Table 7.

The upper limit ($> 3\sigma$) to optical depth of the dust trail is $\tau < 7 \times 10^{-9}$ for Phaethon and $< 2 \times 10^{-8}$ for 1999 YC, respectively. These are broadly comparable to the optical depths of cometary trails (10^{-10} – 10^{-8}) measured by thermal infrared surveys (Sykes & Walker 1992; Reach et al. 2000, 2007). These results are commonly obtained at far distance away ($> 10^4$ km) from the asteroids or nuclei. At much closer distances of $150 \sim 200$ km for Phaethon, on the other hand, we would estimate optical depths three orders of magnitude higher: $\tau < 6 \times 10^{-6}$ (Jewitt et al. 2019). This implies that any larger dust particles ($> 10\mu\text{m}$) are present near the parent body.

We note that optical depths measured at similar wavelengths can be directly compared, because of the similar particle size dependence of the radiating efficiency (Jewitt et al. 2019). While thermal observations ($\lambda > 10\mu\text{m}$) for cometary dust trails have obtained optical depths, those of asteroidal dust trails (bands) (e.g. Nesvorný et al. 2006a,b; Espy Kehoe et al. 2015) and bolides (Borovička et al. 2020) are mostly undetermined. More samples would be helpful for understanding optical depths of asteroidal dust trails.

4.4. Size Limits for Co-moving Objects: *W3*

We searched for possible companions around the PGC-asteroids. Again, the *W3*-images (*WISE*) were used. As in the Figures 4 and 5, no co-moving objects are apparent in our data. The kilometer-sized asteroids would be immediately obvious, while smaller bodies could linger and might just

escape detection. Here we set limits to the brightness of possible co-moving point sources. We put an aperture down in blank regions and measured flux counts and the uncertainty in digital numbers. The aperture area was set to 100 pix^2 ($10 \text{ pix} \times 10 \text{ pix}$), comparable to those of the PGC asteroids. The projected angular distance was set at $\sim 28''$ (10 pix), $56''$ (20 pix) and $84''$ (30 pix) in the North direction from each asteroid (Figures 4 and 5). The corresponding shortest distance is $4.2 \times 10^4 \text{ km}$ from Phaethon and $2.4 \times 10^4 \text{ km}$ from 1999 YC, respectively, which corresponds to far outside of their Hill radii ($\lesssim 60 \text{ km} \approx 0.04''$). Since no distance dependency is found in the measured counts, we applied those of the averaged value to obtain flux density, I_e (in Jy). In order to place the limits to size, we scale them from Phaethon and 1999 YC (see I_n in Table 7, respectively) by assuming that the flux density is proportional only to the cross-sectional area of the radiating body. The derived flux density ratio, I_e/I_n , is $5.8 \pm 0.7 \times 10^{-2}$ in Phaethon and $2.8 \pm 0.4 \times 10^{-2}$ in 1999 YC, respectively. The limiting radius of possible companions, r_e (m), is given by $r_e = 1000 (D_e/2) (I_e/I_n)^{0.5}$. Substituting D_e (Table 3) and I_e/I_n , we obtain the 3σ upper limit to radius of possible co-moving object, $r_e < 650 \text{ m}$ in Figure 4 (Phaethon) and $r_e < 170 \text{ m}$ in Figure 5 (1999 YC), respectively. Objects down to the size limits would be apparent in blank space of the *W3*-images though, undetected.

5. DISCUSSION

5.1. DESTINY⁺ Update

JAXA's DESTINY⁺ mission plans a Phaethon flyby at a relative speed of 36 km s^{-1} either in 2028 January or 2030 November, with a closest approach distance of about 500 km (Ozaki et al. 2022). The DESTINY⁺ dust analyzer (DDA) has the two sensor heads with a total sensitive area, $A_{\text{DDA}} = 0.035 \text{ m}^2$, for collecting interplanetary dust particles (IPDs) with radii $\lesssim 10 \mu\text{m}$ (= a particle mass $\lesssim 10^{-11} \text{ kg}$) (Krüger et al. 2019). But *HST* optical observation reported that the DDA is insufficient for sampling the Geminid meteoroids during the Phaethon flyby (Jewitt et al. 2018). Here we have an update with the thermal observations conducted at the two distinctive distances from Phaethon. One measurement was at the short distance of $150 \sim 200 \text{ km}$ to Phaethon (Jewitt et al. 2019) and another was at the far distances of $50,000 \sim 54,000 \text{ km}$ based on this *WISE* study. We follow the procedure described in Jewitt et al. (2018).

We examined the DESTINY⁺ main-unit and DDA, respectively. Here, we describe the main-unit. The DESTINY⁺ is a cuboid shape having a longitudinal cross section $A_{\text{D}+} < 1.7 \text{ m}^2$ (Naoya Ozaki, private communication)¹⁵. The total cross section of all the particles to be intercepted in this area is $C = \tau A_{\text{D}+}$. This is equal to the maximum cross section of a single, spherical particle having radius $a < (\tau A_{\text{D}+}/\pi)^{1/2}$. The corresponding particle mass is $M = 4/3\pi\rho_d a^3$, where the assumed bulk density $\rho_d = 2000 \text{ kg m}^{-3}$. An upper limit to the number density of dust particles, N_1 (m^{-3}), is placed using either the measured optical depth (τ) as expressed by $N_1 = \tau/(\pi a^2 L)$, or the measured mass-loss rate (Q_{dust}) as expressed by (Equation (3) of Jewitt et al. 2018),

$$N_1 = \frac{1}{4\pi UL^2} \left(\frac{3}{4\pi\rho_d a^3} \right) Q_{\text{dust}}, \quad (8)$$

where a is the maximum radius of dust particles, L is the path length along the line of sight, and U is the speed of released dust particles from Phaethon. We apply $L = 500 \text{ km}$ for the closest

¹⁵ See https://jpn.nec.com/press/202101/20210128_02.html in Japanese

distance of DESTINY⁺ with the measured values of $\tau < 6 \times 10^{-6}$ and $Q_{\text{dust}} \lesssim 14 \text{ kg s}^{-1}$ (Jewitt et al. 2019)¹⁶. Meanwhile, we also apply $L=50,000 \text{ km}$, $\tau < 7 \times 10^{-9}$ (Table 7) and the 3σ upper limit to $Q_{\text{dust}} \lesssim 1 \text{ kg s}^{-1}$ when Phaethon was at $R_{\text{h}}=1 \text{ au}$ (MJD 58104.2148 in Tables 6) from this *WISE* study. $U \sim 3 \text{ ms}^{-1}$ is commonly used for the escape velocity of Phaethon. The average separation between particles, l_a (m), is given by $N_1^{-1/3}$. The expected number of dust particles encountered at the distance L from Phaethon, N_{enc} , is estimated by

$$N_{\text{enc}} \simeq N_1 A_{D+} V_{D+} T_{\text{int}}, \quad (9)$$

where V_{D+} is the flyby speed of DESTINY⁺ and T_{int} is its characteristic interaction time. We adopt $V_{D+} = 36 \text{ km s}^{-1}$ and $T_{\text{int}} \sim 2L/V_{D+}$ to derive N_{enc} . For the DDA case, A_{D+} above is replaced with A_{DDA} . Results are shown in Table 8.

During the closest approach to Phaethon ($L \sim 500 \text{ km}$), DESTINY⁺ is likely to intercept a single millimeter-scale dust particle. DDA would encounter two particles of $500 \mu\text{m}$ in size, though these are beyond its sensitivity or scientific scope. At far distance from Phaethon ($L \sim 50,000 \text{ km}$), a single particle of $200 \mu\text{m}$ in size may hit DESTINY⁺. DDA would also be able to collect six of particles of $10 \mu\text{m}$ -scale with $N_1 \sim 10^{-6} \text{ m}^{-3}$. The derived DDA detectability is consistent with the results examined by the Helios spacecraft measurements and the simulations (IMEX) for 13 cometary trails. Spatial densities of $\sim 10 \mu\text{m}$ -sized particles in the cometary trails of 10^{-8} – 10^{-7} m^{-3} are detectable with an in-situ instrument (Krüger et al. 2020).

This concept is applicable for the case of the Geminid stream, whereas we have a note. Observations of the Geminids find the size range of the meteoroids are from nearly millimeter up to 10s of centimeters (e.g. Blaauw 2017; Yanagisawa et al. 2008, 2021), and even smaller particles $< 1 \text{ mm}$ could be present in the stream. However, much smaller Geminids with $a \lesssim 10 \mu\text{m}$ are swept away from the stream by the radiation pressure (Jewitt & Li 2010; Moorhead 2021) and/or by Poynting-Robertson effect (Ryabova 2012). Such smaller Geminids are probably absent in the stream (See also §3.3 in Jewitt et al. 2018). Thus we conclude that the DESTINY⁺ main-unit may be intercept a modest number of Geminid meteoroids in the trail. DDA is capable of detecting small dust particles, however, they are unlikely to be identified as the Geminids.

5.2. Na Sublimation-driven Mass Production

The essential puzzle for the Geminid stream is its production process from Phaethon. Any measured limiting mass-loss rates for Phaethon are too small to supply the mass of the Geminid stream (See § 4.1). The rates are almost steady and low over nearly the entire orbit. Only at the perihelion the optical brightness is observed to increase suddenly, and the mass-loss rate rises sharply (about a factor of 300) for a short time (STEREO, Jewitt & Hsieh 2022). At perihelion some quasi-episodic dust ejection could have occurred. Here, we focus on the perihelion activity of Phaethon to find a possible mechanism for producing the Geminid meteoroid stream.

The optically-observed recurrent perihelion activity is presumed to be caused by thermal breakdown (fracture and/or desiccation) of rocks, and the release of micron-sized particles at $\sim 3 \text{ kg s}^{-1}$, the slow ejection speeds of $\sim 3 \text{ ms}^{-1}$, and the short tail having mass of $\sim 3 \times 10^5 \text{ kg}$ are reported (Jewitt & Li 2010; Jewitt 2012; Jewitt et al. 2013; Li & Jewitt 2013; Hui & Li 2017). Rotational mass-shedding

¹⁶ We assessed a linear-interpolated τ -value between $L=200 \text{ km}$ (Jewitt et al. 2019) and $L=50,000 \text{ km}$. With the interpolation, we found $\tau < 5.96 \times 10^{-6}$ at $L=500 \text{ km}$. The difference is only $< 0.7\%$ relative to the measured τ at $L=200 \text{ km}$, which is negligibly small. Therefore we used $\tau < 6 \times 10^{-6}$ for the practical value at $L=500 \text{ km}$.

(Nakano & Hirabayashi 2020) and electrostatic force (Jewitt 2012; Jewitt et al. 2015; Kimura et al. 2022) are also proposed as probable mechanisms. But the observed (and modeled) mass-loss rate is tiny and lasted for only ~ 1 day around perihelion (cf. Hui & Li 2017). Even if it occurred at every perihelion return over the dynamical age $\tau_s \sim 1000$ (s) yr, the total ejected mass is about 2×10^8 kg (with a factor of a few uncertainty from the dynamical age). This is more than four to five orders of magnitude too small to be consistent with the stream mass $M_s \approx 10^{13} - 10^{14}$ kg (Hughes & McBride 1989; Blaauw 2017), or what would be expected if Phaethon were comet ($10^{13} - 10^{15}$ kg, Ryabova 2017). Moreover, the micron-sized particles cannot stay in the stream due to their sensitivity to radiation pressure (Jewitt & Li 2010; Moorhead 2021) and/or Poynting-Robertson effect (Ryabova 2012). Larger particles, such as the near mm \sim 10s cm-sized Geminids in the stream, could be simultaneously launched at perihelion but useful data (in longer wavelength) and a mechanism for that launching were absent.

As for the ejection speeds, another consideration is required. Dynamical study requires a catastrophic mass production event to launch larger particles at high ejection speeds of ~ 1 km s $^{-1}$, proposing a comet-like volatile sublimation-driven activity in Phaethon at the smallest $q=0.126$ au about 2,000 yr ago (during one-time perihelion return) (Ryabova 2016, 2018, 2022). This is modeled by the broad width of the stream at $R_h=1$ au from visually observed activities of the Geminid meteor shower (Ryabova & Rendtel 2018). The high-speed ejection is also suggested by the observations of the fine structure of orbits within the Geminid stream (Jiří Borovička, private communication). The fatal problem with proposed comet-like activity is that Phaethon is unlikely to contain icy volatiles (e.g., H $_2$ O, CO, and CO $_2$; see § 4.2) to make the strong pressure needed to launch the dust. Phaethon was unlikely to contain ice 2,000 yr ago, even if it originated from the (icy) inner or outer main-belt asteroids (de León et al. 2010; MacLennan et al. 2021). Sublimation-driven ice-loss models find that the NEAs originating from the inner and outer main-belt would lose ice long before reaching the near-Earth region (Schörghofer et al. 2020; MacLennan et al. 2021). The ice can only possibly be preserved at the polar regions of asteroids having small axial tilts (obliquity) of $\leq 25^\circ$, or the interiors of asteroids with $D_e \geq 10$ km (Schörghofer & Hsieh 2018). A situation such as this is improbable for Phaethon given its small size ($D_e \approx 5-6$ km) and high obliquity of $\gg 25^\circ$ (a pole orientation of $\lambda_e = +85^\circ \pm 13^\circ$ and $\beta_e = -20^\circ \pm 10^\circ$ at ecliptic coordinates (Ansdell et al. 2014)). Furthermore, both of the northern and southern hemispheres have experienced intense solar heating at the smallest $q=0.126$ au by the pole-shift cycles (Hanuš et al. 2016; MacLennan et al. 2021). As such, Phaethon is highly unlikely to contain icy volatiles that could produce the Geminids.

Recently, Masiero et al. (2021) proposed that sublimation of sodium (Na) may drive the perihelion mass-loss activity of Phaethon. Sodium should be or used to be contained in Phaethon and the thermal desorption occurs with intense solar heating, as observed in the Geminids (Kasuga & Jewitt 2019). The near-Sun activity of Phaethon is attributable to emissions from neutral Na-D lines (and Fe I lines), as reported by the STEREO coronagraphic observations (Hui 2022). Here, we examine the Na sublimation-driven mass production to find its consistency with the formation process of the Geminid meteoroid stream.

We focus on the subsurface of Phaethon at the depth $d \sim 0.05$ m. There, maximum sodium sublimation pressure ($\lesssim 1$ Pa) and the temperatures $T_d = 580 \sim 770$ K are modeled using several different

rotational phases at perihelion (Figure (1): Right, Masiero et al. 2021)¹⁷. Sublimation of pure sodium is used in the model as a bounding case, which is not an unrealistic assumption. Sodium is a trace species in rocks and initially would be contained in a silicate mineral phase (e.g. feldspar). However, the pure phase can be made by segregating from the host minerals under severely heated (Čapek & Borovička 2009) or irradiated (Russell & Sanders 1994) conditions like seen in Phaethon approaching very near the Sun (See § 2, Masiero et al. 2021).

We estimate the maximum size of dust particles to be dragged out by sodium sublimation-driven gas. The critical radius of dust particles, a_c , is related with the saturation partial pressure of sodium sublimation over the condensed state, $P_{\text{sat}}(T_d)$ (in Pa) (Equation (2), Masiero et al. 2021), and given by (Jewitt 2002),

$$a_c \sim \frac{9C_D P_{\text{sat}}(T_d)}{8\pi G \rho_d^2 D_e}, \quad (10)$$

where $C_D \sim 1$ is the dimensionless drag coefficient, $G = 6.67 \times 10^{-11} \text{ m}^3 \text{ kg}^{-1} \text{ s}^{-2}$ is the gravitational constant, and the same values of $\rho_d = 2000 \text{ kg m}^{-3}$ and $D_e = 4.6 \text{ km}$ (from Phaethon) are adopted. With $T_d = 580 \sim 770 \text{ K}$, we obtain $P_{\text{sat}}(T_d) = 0.003 \sim 0.6 \text{ Pa}$. The corresponding critical radius is $a_c \sim 0.09 \sim 17 \text{ cm}$, comparable to the optically measured size of the Geminid meteoroids in lunar impacts (e.g. $\lesssim 20 \text{ cm}$, Yanagisawa et al. 2008, 2021). By comparison we set $\rho_d = 3000 \text{ kg m}^{-3}$ estimated from the observations of the Geminid meteors (Babadzhanov & Kokhirova 2009) to find $a_c \sim 0.04 \sim 7 \text{ cm}$, rather consistent to the measured Geminids sizes (cf. Blaauw 2017; Yanagisawa et al. 2008, 2021). For the particles around the rotational equator, a_c would be larger due to rotation assist by the enhanced angular velocity (Jewitt 2002), therefore we consider our estimations as useful lower limit. The thermal speed for gas of sodium atoms, V_{gas} , is given by (Equation (10) of Graykowski & Jewitt 2019),

$$V_{\text{gas}}(T_d) = \sqrt{\frac{8k_B T_d}{\pi \mu m_H}}, \quad (11)$$

where $k_B = 1.38 \times 10^{-23} \text{ J K}^{-1}$ is the Boltzmann constant, $\mu = 22.99$ is the molecular weight of sodium, $m_H = 1.67 \times 10^{-27} \text{ kg}$ is the mass of the hydrogen atom, and T_d (in K) is the temperature at the depth of 0.05 m below the Phaethon surface. Substituting $T_d = 580 \sim 770 \text{ K}$, we find $V_{\text{gas}}(T_d) = 730 \sim 840 \text{ m s}^{-1}$. This is orders of magnitude faster than the other proposed production processes (e.g. thermal breakdown), and comparable to the required speeds of $\sim 1 \text{ km s}^{-1}$ described by Ryabova (2016).

Next, we estimate the total mass of dust particles ejected by the sodium sublimation-driven activity to compare with the Geminid stream mass. The total specific sublimation mass-loss rate of sodium at depth $d \sim 0.05 \text{ m}$, $(dm/dt)_d$ in $\text{kg m}^{-2} \text{ s}^{-1}$, is given by integrating over temperatures $580 \lesssim T_d \lesssim 770 \text{ K}$. The dust-to-gas (sodium) mass ratio ~ 1 is applied (Oppenheimer 1980). Then we obtain

$$\left(\frac{dm}{dt}\right)_d = \int \frac{P_{\text{sat}}(T_d)}{V_{\text{gas}}(T_d)} dT_d. \quad (12)$$

Adopting $P_{\text{sat}}(T_d)$ (Masiero et al. 2021) and Equation (11), we find $(dm/dt)_d \sim 0.03 \text{ kg m}^{-2} \text{ s}^{-1}$. The mass-loss rate from the entire subsurface of Phaethon ($\sim \pi D_e^2$) corresponds to $\sim 2.0 \times 10^6 \text{ kg s}^{-1}$. If

¹⁷ NIMBUS (Numerical Icy Minor Body evolUtion Simulator) is the thermophysical model developed by Davidsson et al. (2022). The calculation considers a rotating spherical body consisting of a porous mixture of dust and ice, and tracks the internal ice sublimation, vapor condensation, and diffusion of gas and heat in the radial and latitudinal directions over time during body rotation (See also, Davidsson et al. 2021).

a Na-driven perihelion activity likewise lasted for 1 day each orbital return, the total mass over the dynamical age $\tau_s \sim 1000(\text{s})\text{yr}$ is 1.2×10^{14} kg (with a factor of a few uncertainty from the dynamical age). This is consistent with the Geminid stream mass $M_s \approx 10^{13} - 10^{14}$ kg (Hughes & McBride 1989; Blaauw 2017), and also is comparable to that of the hypothetical cometary nature for Phaethon ($M_s \approx 10^{13} - 10^{15}$ kg, Ryabova 2017). We note that the calculated Na-driven perihelion mass-loss rate is about five or six orders of magnitude larger than the measured mass-loss rates for Phaethon in the optical, near- and mid-infrared wavelengths (§ 4.1). For example, the STEREO optically estimated the perihelion mass-loss rates 0.01 kg s^{-1} ($= 10^3 \text{ kg} / 1 \text{ day}$) (Hui 2022), up to $\sim 3 \text{ kg s}^{-1}$ (Jewitt & Hsieh 2022). These measured values are associated with the $1 \sim 10 \mu\text{m}$ -sized particles. On the other hand, the calculated Na-driven perihelion mass-loss rate is presumably related to the near mm \sim 10s cm-sized particles containing more mass. We again propose longer wavelength observations aimed at detecting larger particles, especially during the perihelion activity of Phaethon.

We also note that there should be a mechanism to replenish sodium-depleted subsurface with sodium-rich layer every return, but unknown yet (Jewitt & Hsieh 2022). A single perihelion passage obviously results in the depletion of sodium abundance down to the depth $d \lesssim 0.05$ m (Figure (2): Middle left, Masiero et al. 2021). How had the sodium been supplied into the subsurface for the stream lifetime $\tau_s \sim 1000(\text{s})\text{yr}$? As a hypothesis, combinations of the suggested active-triggers are considerable. Thermal breakdown will be concentrated in thin surface layer having thickness similar to the diurnal thermal skin depth $d_s \sim 0.1$ m (Jewitt & Li 2010), comparable within a factor of two in the sodium-driver model case. The material would be found in thin layer accessible to thermal wave, which would be disintegrating and peeled off, resulting in a renewal as fresh surface with sodium. Still, there remains unknown parameters (e.g. lifetime of thin surface layer) and a combination of activity mechanisms may be needed to advance our understanding. Future work will investigate a scenario where Phaethon's nature is most likely an asteroid with some of the mass production attributable to a past breakup, while the sodium can play a contributory role of comet-like activity at perihelion.

6. SUMMARY

We present *WISE*/*NEOWISE* observations of the potentially Geminid-associated asteroids, Phaethon, 2005 UD and 1999 YC. The multi-epoch thermal infrared data are obtained in the wavelength bands $3.4 \mu\text{m}$ (*W1*), $4.6 \mu\text{m}$ (*W2*), $12 \mu\text{m}$ (*W3*) and $22 \mu\text{m}$ (*W4*). The asteroids appear point-like in all image data. We use the data to set limits to the presence of dust attributable to the asteroids. The decade-long survey data give the following results.

1. No evidence of lasting mass-loss was found in the Phaethon image. The maximum dust production rate is $Q_{\text{dust}} \lesssim 2 \text{ kg s}^{-1}$, having no strong dependency on heliocentric distance at $R_{\text{h}} = 1.0 - 2.3$ au.
2. The measured limiting dust production rates are orders of magnitude too small to supply the mass of the Geminid meteoroid stream in the 1000(s) yr dynamical age. If Phaethon is the source of the Geminids, the stream mass is likely to be produced episodically, not in steady-state.
3. No dust trail is detected around Phaethon when at $R_{\text{h}} = 2.3$ au. The corresponding upper limit to the optical depth is $\tau < 7 \times 10^{-9}$.

4. No co-moving objects were detected. The limiting radius of a possible source is $r_e < 650$ m at 42,000 km distance to Phaethon.
5. When DESTINY⁺ passes at 50,000 km distance from Phaethon, several of 10 μ m-scale particles would be captured by the dust analyzer, though they most likely will not be identified as the Geminids. During the flyby phase (at 500 km distance), two particles of 500 μ m in size are encountered in the instrument.
6. The 2005 UD image found no extended emission for on-going mass-loss. The maximum limit to the dust production rate is $Q_{\text{dust}} \lesssim 0.1 \text{ kg s}^{-1}$ at $R_h=1.0\text{--}1.4$ au. If dust production were sustained over the $\sim 10,000$ yr dynamical age of the Daytime Sextantid meteoroid stream, the mass of the stream is $\sim 10^{10}$ kg. If it were produced by the catastrophic event, the stream mass would be more.
7. The 1999 YC data showed no coma at $R_h=1.0\text{--}1.6$ au. The maximum mass-loss rate is $Q_{\text{dust}} \lesssim 0.1 \text{ kg s}^{-1}$.
8. No dust trail associated with 1999 YC was found at $R_h=1.6$ au, corresponding to the upper limit to the optical depth $\tau < 2 \times 10^{-8}$.
9. No associated-fragments with radii $r_e < 170$ m were discovered at 24,000 km distance from 1999 YC.
10. The sodium sublimation-driven perihelion activity of Phaethon is expected to eject the near mm \sim 10s cm-sized dust particles at speeds of 730–840 m s⁻¹ through gas drag. A mass-loss rate $\sim 2.0 \times 10^6 \text{ kg s}^{-1}$, if allowed to last for 1 day every return, would deliver about 1.2×10^{14} kg in 1000(s) yr. These processes are compatible with the structure of the Geminid meteoroid stream. For this mechanism to be plausible, though, a sustainable mechanism to resupply sodium-depleted subsurface with sodium-rich minerals is required.

We are grateful to David Jewitt for productive discussion. TK thanks Mikiya Sato, Chie Tsuchiya, Sunao Hasegawa, Naoya Ozaki, Galina Ryabova, Yung Kipreos, Peter Brown, Jiří Borovička, Björn J. R. Davidsson, Hideyo Kawakita, and Jun-ichi Watanabe for support. This publication makes use of data products from the *Wide-field Infrared Survey Explorer*, which is a joint project of the University of California, Los Angeles, and the Jet Propulsion Laboratory/California Institute of Technology, funded by the National Aeronautics and Space Administration. Also, this publication makes use of data products from the Near-Earth Object Wide-field Infrared Survey Explorer (NEOWISE), which is a joint project of the Jet Propulsion Laboratory/California Institute of Technology and the University of Arizona. NEOWISE is funded by the National Aeronautics and Space Administration. This publication uses data obtained from the NASA Planetary Data System (PDS). This research has made use of data and services provided by the International Astronomical Union’s Minor Planet Center. This research has made use of the NASA/IPAC Infrared Science Archive, which is funded by the National Aeronautics and Space Administration and operated by the California Institute of Technology, under contract with the National Aeronautics and Space Administration. We would like to address special thanks to anonymous reviewer and to Maria Womack for scientific editor. Finally, we express deep gratitude to Althea Moorhead, Margaret Campbell-Brown and the LOC members for Meteoroids 2022 (held in Virtual) providing opportunity to enhance this study.

Facilities: WISE, NEOWISE

REFERENCES

- A'Hearn, M. F., Schleicher, D. G., Millis, R. L., Feldman, P. D., & Thompson, D. T. 1984, *AJ*, 89, 579
- Ansdell, M., Meech, K. J., Hainaut, O., et al. 2014, *ApJ*, 793, 50
- Arendt, R. G. 2014, *AJ*, 148, 135
- Babadzhanov, P. B., & Kokhirova, G. I. 2009, *A&A*, 495, 353
- Bauer, J. M., Choi, Y.-J., Weissman, P. R., et al. 2008, *PASP*, 120, 393
- Bauer, J. M., Gicquel, A., Kramer, E., & Meech, K. J. 2021, *PSJ*, 2, 34
- Bauer, J. M., Walker, R. G., Mainzer, A. K., et al. 2011, *ApJ*, 738, 171
- Bauer, J. M., Stevenson, R., Kramer, E., et al. 2015, *ApJ*, 814, 85
- Blaauw, R. C. 2017, *Planet. Space Sci.*, 143, 83
- Bockelée-Morvan, D., Brooke, T. Y., & Crovisier, J. 1995, *Icarus*, 116, 18
- Borovička, J. 2001, in *ESA Special Publication*, Vol. 495, *Meteoroids 2001 Conference*, ed. B. Warmbein, 203–208
- Borovička, J., Kotten, P., Spurný, P., Boček, J., & Štork, R. 2005, *Icarus*, 174, 15
- Borovička, J., Macke, R. J., Campbell-Brown, M. D., et al. 2019, in *Meteoroids: Sources of Meteors on Earth and Beyond*, ed. G. O. Ryabova, D. J. Asher, & M. J. Campbell-Brown, 37
- Borovička, J., Setvák, M., Roesli, H., & Kerkmann, J. K. 2020, *A&A*, 644, A58
- Bouziani, N., & Jewitt, D. 2022, *ApJ*, 924, 37
- Bowell, E., Hapke, B., Domingue, D., et al. 1989, in *Asteroids II*, ed. R. P. Binzel, T. Gehrels, & M. S. Matthews, 524–556
- Bus, S. J., & Binzel, R. P. 2002, *Icarus*, 158, 146
- Čapek, D., & Borovička, J. 2009, *Icarus*, 202, 361
- Cepplecha, Z., Borovička, J., Elford, W. G., et al. 1998, *SSRv*, 84, 327
- Chamberlin, A. B., McFadden, L.-A., Schulz, R., Schleicher, D. G., & Bus, S. J. 1996, *Icarus*, 119, 173
- Cutri, R. M., Wright, E. L., Conrow, T., et al. 2012, *Explanatory Supplement to the WISE All-Sky Data Release Products*, *Explanatory Supplement to the WISE All-Sky Data Release Products*, ,
- Cutri, R. M., Mainzer, A., Conrow, T., et al. 2015, *Explanatory Supplement to the NEOWISE Data Release Products*, *Explanatory Supplement to the NEOWISE Data Release Products*, ,
- Davidsson, B. J. R., Samarasinha, N. H., Farnocchia, D., & Gutiérrez, P. J. 2022, *MNRAS*, 509, 3065
- Davidsson, B. J. R., Birch, S., Blake, G. A., et al. 2021, *Icarus*, 354, 114004
- de León, J., Campins, H., Tsiganis, K., Morbidelli, A., & Licandro, J. 2010, *A&A*, 513, A26
- Devogèle, M., MacLennan, E., Gustafsson, A., et al. 2020, *PSJ*, 1, 15
- Dunham, D. W., Dunham, J. B., Buie, M., et al. 2019, in *LPI Contributions*, Vol. 2189, *Asteroid Science in the Age of Hayabusa2 and OSIRIS-REx*, 2062
- Espy Kehoe, A. J., Kehoe, T. J. J., Colwell, J. E., & Dermott, S. F. 2015, *ApJ*, 811, 66
- Graykowski, A., & Jewitt, D. 2019, *AJ*, 158, 112
- Gustafson, B. A. S. 1989, *A&A*, 225, 533
- Hanuš, J., Delbo', M., Vokrouhlický, D., et al. 2016, *A&A*, 592, A34
- Hanuš, J., Vokrouhlický, D., Delbo', M., et al. 2018, *A&A*, 620, L8
- Harris, A. W. 1998, *Icarus*, 131, 291
- Harvey, G. A. 1973, *NASA Special Publication*, 319, 103
- Hovis, W. A., J., & Callahan, W. R. 1966, *Journal of the Optical Society of America (1917-1983)*, 56, 639
- Hsieh, H. H., & Haghhighipour, N. 2016, *Icarus*, 277, 19
- Hsieh, H. H., & Jewitt, D. 2005, *ApJ*, 624, 1093
- Hughes, D. W., & McBride, N. 1989, *MNRAS*, 240, 73
- Hui, M.-T. 2022, *arXiv e-prints*, arXiv:2206.09704
- Hui, M.-T., & Li, J. 2017, *AJ*, 153, 23

- Hung, D., Hanuš, J., Masiero, J. R., & Tholen, D. J. 2022, *PSJ*, 3, 56
- Jakubík, M., & Neslušan, L. 2015, *MNRAS*, 453, 1186
- Jakubík, M., & Neslušan, L. 2015, *MNRAS*, 453, 1186
- Jarrett, T. H., Cohen, M., Masci, F., et al. 2011, *ApJ*, 735, 112
- Jewitt, D. 2012, *AJ*, 143, 66
- Jewitt, D., Asmus, D., Yang, B., & Li, J. 2019, *AJ*, 157, 193
- Jewitt, D., & Hsieh, H. 2006, *AJ*, 132, 1624
- Jewitt, D., Hsieh, H., & Agarwal, J. 2015, in *Asteroids IV*, ed. P. Michel, F. E. DeMeo, & W. F. Bottke (University of Arizona Press), 221–241
- Jewitt, D., & Hsieh, H. H. 2022, arXiv e-prints, arXiv:2203.01397
- Jewitt, D., & Kalas, P. 1998, *ApJL*, 499, L103
- Jewitt, D., & Li, J. 2010, *AJ*, 140, 1519
- Jewitt, D., Li, J., & Agarwal, J. 2013, *ApJL*, 771, L36
- Jewitt, D., & Luu, J. 1992, *AJ*, 104, 398
- Jewitt, D., Mutchler, M., Agarwal, J., & Li, J. 2018, *AJ*, 156, 238
- Jewitt, D. C. 2002, *AJ*, 123, 1039
- Joepok, T. J., & Jenniskens, P. M. 2011, in *Meteoroids: The Smallest Solar System Bodies*, ed. M. D. E. H. B. F. Cooke, W. J. & D. Janches (Colorado, USA: Proceedings of the Meteoroids Conference held in Breckenridge, NASA/CP-2011-216469), 7–13
- Kareta, T., Reddy, V., Pearson, N., Sanchez, J. A., & Harris, W. M. 2021, *PSJ*, 2, 190
- Kasuga, T., & Jewitt, D. 2008, *AJ*, 136, 881
- . 2019, in *Meteoroids: Sources of Meteors on Earth and Beyond*, Ryabova G. O., Asher D. J., and Campbell-Brown M. D. (eds.), Cambridge, UK: Cambridge University Press, 336 pp., ISBN 9781108426718, 2019, p. 187-209, 187
- Kasuga, T., Watanabe, J., & Ebizuka, N. 2005, *A&A*, 438, L17
- Kasuga, T., Yamamoto, T., Kimura, H., & Watanabe, J. 2006, *A&A*, 453, L17
- Kimura, H., Ohtsuka, K., Kikuchi, S., et al. 2022, *Icarus*, 382, 115022
- Krüger, H., Strub, P., Sommer, M., et al. 2020, *A&A*, 643, A96
- Krüger, H., Strub, P., Srama, R., et al. 2019, *Planet. Space Sci.*, 172, 22
- Lebofsky, L. A., & Spencer, J. R. 1989, in *Asteroids II*, ed. R. P. Binzel, T. Gehrels, & M. S. Matthews, 128–147
- Lebofsky, L. A., Sykes, M. V., Tedesco, E. F., et al. 1986, *Icarus*, 68, 239
- Li, J., & Jewitt, D. 2013, *AJ*, 145, 154
- . 2015, *AJ*, 149, 133
- Lindblad, B. A. 1987, in *The Evolution of the Small Bodies of the Solar System*, ed. M. Fulchignoni & L. Kresak, 229
- Luu, J. X., & Jewitt, D. C. 1992, *Icarus*, 97, 276
- MacLennan, E., Marshall, S., & Granvik, M. 2022, arXiv e-prints, arXiv:2203.08865
- MacLennan, E., Toliou, A., & Granvik, M. 2021, *Icarus*, 366, 114535
- MacLennan, E. M., & Emery, J. P. 2021, *PSJ*, 2, 161
- Madiedo, J. M., Ortiz, J. L., Yanagisawa, M., Aceituno, J., & Aceituno, F. 2019, in *Meteoroids: Sources of Meteors on Earth and Beyond*, ed. G. O. Ryabova, D. J. Asher, & M. J. Campbell-Brown, 136
- Mainzer, A., Grav, T., Masiero, J., et al. 2011, *ApJ*, 736, 100
- Mainzer, A., Bauer, J., Cutri, R. M., et al. 2014, *ApJ*, 792, 30
- Mainzer, A. K., Bauer, J. M., Cutri, R. M., et al. 2019, *NASA Planetary Data System*, doi:10.26033/18S3-2Z54
- Masiero, J. R., Davidsson, B. J. R., Liu, Y., Moore, K., & Tuite, M. 2021, *PSJ*, 2, 165
- Masiero, J. R., Wright, E. L., & Mainzer, A. K. 2019, *AJ*, 158, 97
- Masiero, J. R., Mainzer, A. K., Grav, T., et al. 2011, *ApJ*, 741, 68
- Masiero, J. R., Redwing, E., Mainzer, A. K., et al. 2018, *AJ*, 156, 60
- Masiero, J. R., Mainzer, A. K., Bauer, J. M., et al. 2020, *PSJ*, 1, 5
- Mommert, M., Jedicke, R., & Trilling, D. E. 2018, *AJ*, 155, 74
- Moorhead, A. V. 2021, *Icarus*, 354, 113949
- Nakano, R., & Hirabayashi, M. 2020, *ApJL*, 892, L22
- NEOWISE Team. 2020, *NEOWISE-R Single Exposure (L1b) Source Table*, IPAC, doi:10.26131/IRSA144.
<https://catcopy.ipac.caltech.edu/does/doi.php?id=10.26131>
- Nesvorný, D., Vokrouhlický, D., Bottke, W. F., & Sykes, M. 2006a, *Icarus*, 181, 107

- Nesvorný, D., Sykes, M., Lien, D. J., et al. 2006b, *AJ*, 132, 582
- Nugent, C. R., Mainzer, A., Masiero, J., et al. 2015, *ApJ*, 814, 117
- Ohtsuka, K., Arakida, H., Ito, T., Yoshikawa, M., & Asher, D. J. 2008, *Meteoritics and Planetary Science Supplement*, 43, 5055
- Ohtsuka, K., Sekiguchi, T., Kinoshita, D., et al. 2006, *A&A*, 450, L25
- Ootsubo, T., Kawakita, H., Hamada, S., et al. 2012, *ApJ*, 752, 15
- Oppenheimer, M. 1980, *ApJ*, 240, 923
- Ozaki, N., Yamamoto, T., Gonzalez-Franquesa, F., et al. 2022, *Acta Astronautica*, 196, 42
- Pittichová, J., Woodward, C. E., Kelley, M. S., & Reach, W. T. 2008, *AJ*, 136, 1127
- Prialnik, D., Benkhoff, J., & Podolak, M. 2004, *Modeling the structure and activity of comet nuclei*, ed. M. C. Festou, H. U. Keller, & H. A. Weaver, 359
- Reach, W. T., Kelley, M. S., & Sykes, M. V. 2007, *Icarus*, 191, 298
- Reach, W. T., Kelley, M. S., & Vaubaillon, J. 2013, *Icarus*, 226, 777
- Reach, W. T., Sykes, M. V., Lien, D., & Davies, J. K. 2000, *Icarus*, 148, 80
- Rosser, J. D., Bauer, J. M., Mainzer, A. K., et al. 2018, *AJ*, 155, 164
- Russell, D. P., & Sanders, M. 1994, *Radiation Effects and Defects in Solids*, 132, 119
- Ryabova, G. O. 1999, *Solar System Research*, 33, 224
- . 2012, *MNRAS*, 423, 2254
- . 2016, *MNRAS*, 456, 78
- . 2017, *Planetary and Space Science*, 143, 125
- . 2018, *MNRAS*, 479, 1017
- . 2022, *Planet. Space Sci.*, 210, 105378
- Ryabova, G. O., & Rendtel, J. 2018, *MNRAS*, 475, L77
- Schörghofer, N., & Hsieh, H. H. 2018, *Journal of Geophysical Research (Planets)*, 123, 2322
- Schörghofer, N., Hsieh, H. H., Novaković, B., & Walsh, K. J. 2020, *Icarus*, 348, 113865
- Springmann, A., Lauretta, D. S., Klaue, B., et al. 2019, *Icarus*, 324, 104
- Sykes, M. V., & Walker, R. G. 1992, *Icarus*, 95, 180
- Szalay, J. R., Pokorný, P., Jenniskens, P., & Horányi, M. 2018, *MNRAS*, 474, 4225
- Tancredi, G. 2014, *Icarus*, 234, 66
- Taylor, P. A., Rivera-Valentín, E. G., Benner, L. A. M., et al. 2019, *Planet. Space Sci.*, 167, 1
- Tedesco, E. F., Noah, P. V., Noah, M., & Price, S. D. 2004, *NASA Planetary Data System, IRAS*
- Todorović, N. 2018, *MNRAS*, 475, 601
- Trigo-Rodríguez, J. M., Llorca, J., Borovicka, J., & Fabregat, J. 2003, *Meteoritics and Planetary Science*, 38, 1283
- Uchiyama, S. 2010, *WGN, Journal of the International Meteor Organization*, 38, 31
- Vaubaillon, J., Neslušan, L., Sekhar, A., Rudawska, R., & Ryabova, G. O. 2019, *From Parent Body to Meteor Shower: The Dynamics of Meteoroid Streams*, 161
- Whipple, F. L. 1983, *IAU Circ.*, 3881
- Wiegert, P. A., Houde, M., & Peng, R. 2008, *Icarus*, 194, 843
- Williams, I. P., & Wu, Z. 1993, *MNRAS*, 262, 231
- WISE Team. 2020a, *WISE All-Sky Single Exposure (L1b) Source Table, IPAC*, doi:10.26131/IRSA139.
<https://catcopy.ipac.caltech.edu/doi/doi.php?id=10.26131/IRSA139>
- . 2020b, *WISE 3-Band Cryo Single Exposure (L1b) Source Table, IPAC*, doi:10.26131/IRSA127.
<https://catcopy.ipac.caltech.edu/doi/doi.php?id=10.26131/IRSA127>
- . 2020c, *NEOWISE 2-Band Post-Cryo Single Exposure (L1b) Source Table, IPAC*, doi:10.26131/IRSA124.
<https://catcopy.ipac.caltech.edu/doi/doi.php?id=10.26131/IRSA124>
- Wright, E., Mainzer, A., Masiero, J., et al. 2018, arXiv e-prints, arXiv:1811.01454
- Wright, E. L., Eisenhardt, P. R. M., Mainzer, A. K., et al. 2010, *AJ*, 140, 1868
- Yanagisawa, M., Ikegami, H., Ishida, M., et al. 2008, *Meteoritics and Planetary Science Supplement*, 43, 5169
- Yanagisawa, M., Uchida, Y., Kurihara, S., et al. 2021, *Planet. Space Sci.*, 195, 105131
- Yu, L. L., Ip, W. H., & Spohn, T. 2019, *MNRAS*, 482, 4243

Table 1. *WISE*/NEOWISE Observation Log

Object	MJD ^a	UT Date	RA ^b	DEC ^c	R _h ^d	Δ ^e	α ^f	W1 ^g	W2 ^h	W3 ⁱ	W4 ^j
			(deg)	(deg)	(AU)	(AU)	(deg)	(mag)	(mag)	(mag)	(mag)
Phaethon	55203.2564●	2010-Jan-07	9.79	+22.58	2.3171	2.0755	25.1	16.995	15.599	8.736±0.052	6.155±0.113
	55203.3888●	2010-Jan-07	9.81	+22.57	2.3175	2.0778	25.1	16.859±0.464	15.108	8.700±0.048	6.050±0.115
	57035.2144	2015-Jan-13	21.68	+16.90	1.3292	0.8307	47.6	14.259±0.075	11.229±0.028	—	—
	57035.2801	2015-Jan-13	21.66	+16.87	1.3283	0.8309	47.6	14.467±0.074	11.361±0.024	—	—
	57035.4115	2015-Jan-13	21.62	+16.82	1.3266	0.8315	47.7	14.266±0.076	11.382±0.027	—	—
	57035.5429	2015-Jan-13	21.58	+16.76	1.3249	0.8320	47.8	14.375±0.083	11.349±0.026	—	—
	57035.6743	2015-Jan-13	21.54	+16.71	1.3232	0.8325	47.9	14.300±0.061	11.288±0.024	—	—
	57663.4184	2016-Oct-02	236.56	+84.32	1.0793	0.4055	68.0	12.403±0.025	9.214±0.014	—	—
	57663.5494	2016-Oct-02	239.60	+84.37	1.0813	0.4057	67.7	12.478±0.031	9.238±0.014	—	—
	57663.6149	2016-Oct-02	241.14	+84.40	1.0824	0.4059	67.6	12.425±0.026	9.233±0.014	—	—
58024.3765	2017-Sep-28	96.73	+33.36	1.9047	1.6289	31.7	15.775±0.197	14.171±0.184	—	—	
58104.2148★	2017-Dec-17★	3.77	+25.01	1.0068	0.0691	68.9	7.782±0.041†	4.224±0.221†	—	—	
2005 UD	57750.3946	2016-Dec-28	357.82	+47.19	1.3650	0.7818	45.1	15.236±0.118	13.693±0.104	—	—
	58383.2977	2018-Sep-22	90.04	+5.90	1.0291	0.2456	77.2	13.907±0.053	10.716±0.020	—	—
	58383.4286	2018-Sep-22	89.60	+5.94	1.0312	0.2447	76.7	14.199±0.058	10.917±0.024	—	—
	58383.4941	2018-Sep-22	89.38	+5.96	1.0323	0.2443	76.5	13.829±0.058	10.697±0.021	—	—
	58821.4792	2019-Dec-04	234.89	+67.36	1.0970	0.4768	64.0	15.505±0.136	12.519±0.057	—	—
	58821.6099	2019-Dec-04	235.42	+67.16	1.0950	0.4759	64.2	15.255±0.156	12.435±0.051	—	—
	58821.7408	2019-Dec-04	235.93	+66.96	1.0930	0.4750	64.4	15.899±0.201	12.477±0.055	—	—
	58821.8716	2019-Dec-04	236.44	+66.76	1.0910	0.4741	64.6	15.689±0.150	12.740±0.054	—	—
1999 YC	55213.2458	2010-Jan-17	27.957	+15.923	1.6242	1.2137	37.1	16.303	14.893±0.317	8.733±0.055	6.353±0.155
	55213.5766	2010-Jan-17	27.886	+15.953	1.6208	1.2157	37.2	17.094	14.890	9.517±0.105	7.178±0.298
	55213.6428*	2010-Jan-17	27.872	+15.959	1.6201	1.2161	37.3	16.776	14.760±0.261	8.953±0.065	6.650±0.186
	55213.7089*	2010-Jan-17	27.858	+15.965	1.6194	1.2165	37.3	◇	◇	8.834±0.060	6.636±0.184
	55213.7751*	2010-Jan-17	27.844	+15.971	1.6187	1.2169	37.3	16.999	14.841	9.428±0.099	7.125±0.287
	55213.8413*	2010-Jan-17	27.830	+15.977	1.6180	1.2173	37.3	16.964	14.539±0.227	9.009±0.070	6.716±0.204
	55213.9736	2010-Jan-17	27.802	+15.989	1.6166	1.2181	37.4	16.507	14.756	9.174±0.080	6.853±0.229
	57738.0234	2016-Dec-16	277.30	+66.69	1.0178	0.2500	75.2	13.623±0.043	10.478±0.02	—	—

NOTE—Cases where no measurement was available from NEOWISE is indicated as “—”. Entries without uncertainties indicate a 2σ upper limit extracted using the *WISE* photometric pipeline.

^a Modified Julian Date of the mid-point of the observation.

^b Right ascension (J2000).

^c Declination (J2000).

^d Heliocentric distance.

^e *WISE*-centric distance.

^f Phase angle.

^g Magnitude at W1.

^h Magnitude at W2.

ⁱ Magnitude at W3.

^j Magnitude at W4.

● The W3 images are combined into Figure 4. * The W3 images are combined into Figure 5. ★ Phaethon’s closest approach date to the Earth. † Saturated photometric biases were corrected from the source data of W1=7.745±0.014 mag and W2=2.894±0.003 mag following Equation (1). ◇ Contaminated by a star.

Table 2. Orbital Properties

Object	a^a	e^b	i^c	q^d	ω^e	Ω^f	Q^g	P_{orb}^h	T_J^i
	(AU)		(deg)	(AU)	(deg)	(deg)	(AU)	(yr)	
Phaethon	1.271	0.890	22.255	0.140	322.175	265.223	2.403	1.43	4.509
2005 UD	1.275	0.872	28.664	0.163	207.597	19.716	2.387	1.44	4.504
1999 YC	1.422	0.830	38.217	0.241	156.393	64.793	2.603	1.70	4.115

NOTE—Orbital data were obtained from NASA JPL Small-Body Database (Epoch 2459600.5: 2022-Jan-21)

^aSemimajor axis.

^bEccentricity.

^cInclination.

^dPerihelion distance.

^eArgument of perihelion.

^fLongitude of ascending node.

^gAphelion distance.

^hOrbital period.

ⁱTisserand parameter with respect to Jupiter. $T_J > 3.08$ for asteroids and $T_J < 3.08$ for comets, given $a < a_J = 5.2$ au (Jewitt et al. 2015). See also, other suggested comet-asteroid thresholds of $T_J = 3.05$ (Tancredi 2014) and $T_J = 3.10$ (Hsieh & Haghhighipour 2016) (Reviewed in Jewitt & Hsieh 2022).

Table 3. Effective diameter and geometric visible albedo determined from *WISE*/NEOWISE.

Object	D_e^a (km)	p_v^b	Source
Phaethon	$4.6^{+0.2}_{-0.3}*$	0.16 ± 0.02	(1)
2005 UD	1.2 ± 0.4	0.14 ± 0.09	(1)
1999 YC	1.7 ± 0.2	0.09 ± 0.03	(2)

^aEffective spherical diameter.

^bGeometric visible albedo.

*The uncertainty used in this work is ± 0.3 km
(see § 2).

References—(1) [Masiero et al. \(2019\)](#); (2) [Mainzer et al. \(2019\)](#)

Table 4. Thermal Flux Density

Object	MJD ^a	W1 ^b (Jy)	W2 ^c (Jy)	W3 ^d (Jy)	W4 ^e (Jy)
Phaethon	55203.2564	1.87×10^{-6}	4.73×10^{-5}	$9.09 \pm 1.73 \times 10^{-3}$	$2.93 \pm 0.62 \times 10^{-2}$
	55203.3888	$4.52 \pm 2.10 \times 10^{-6}$	8.44×10^{-5}	$9.40 \pm 1.78 \times 10^{-3}$	$3.23 \pm 0.69 \times 10^{-2}$
	57035.2144	$8.33 \pm 1.64 \times 10^{-5}$	$4.27 \pm 0.79 \times 10^{-3}$	—	—
	57035.2801	$2.15 \pm 0.42 \times 10^{-5}$	$3.76 \pm 0.70 \times 10^{-3}$	—	—
	57035.4115	$8.35 \pm 1.65 \times 10^{-5}$	$3.68 \pm 0.68 \times 10^{-3}$	—	—
	57035.5429	$5.01 \pm 1.00 \times 10^{-5}$	$3.81 \pm 0.71 \times 10^{-3}$	—	—
	57035.6743	$7.30 \pm 1.41 \times 10^{-5}$	$4.04 \pm 0.75 \times 10^{-3}$	—	—
	57663.4184	$1.11 \pm 0.21 \times 10^{-3}$	$2.98 \pm 0.55 \times 10^{-2}$	—	—
	57663.5494	$9.49 \pm 1.77 \times 10^{-4}$	$2.90 \pm 0.54 \times 10^{-2}$	—	—
	57663.6149	$1.05 \pm 0.20 \times 10^{-3}$	$2.92 \pm 0.54 \times 10^{-2}$	—	—
	58024.3765	$3.04 \pm 0.79 \times 10^{-5}$	$2.35 \pm 0.59 \times 10^{-4}$	—	—
58104.2148*	0.12 ± 0.02	3.07 ± 0.84	—	—	
2005 UD	57750.3946	$1.24 \pm 1.16 \times 10^{-4}$	$4.47 \pm 4.18 \times 10^{-4}$	—	—
	58383.2977	$4.21 \pm 3.92 \times 10^{-4}$	$7.69 \pm 7.16 \times 10^{-3}$	—	—
	58383.4286	$2.80 \pm 2.61 \times 10^{-4}$	$6.36 \pm 5.92 \times 10^{-3}$	—	—
	58383.4941	$4.60 \pm 4.29 \times 10^{-4}$	$7.82 \pm 7.28 \times 10^{-3}$	—	—
	58821.4792	$7.45 \pm 6.99 \times 10^{-5}$	$1.41 \pm 1.31 \times 10^{-3}$	—	—
	58821.6099	$1.08 \pm 1.02 \times 10^{-4}$	$1.53 \pm 1.43 \times 10^{-3}$	—	—
	58821.7408	$3.62 \pm 3.43 \times 10^{-5}$	$1.47 \pm 1.37 \times 10^{-3}$	—	—
	58821.8716	$5.46 \pm 5.14 \times 10^{-5}$	$1.15 \pm 1.07 \times 10^{-3}$	—	—
1999 YC	55213.2458	4.11×10^{-5}	$1.40 \pm 0.70 \times 10^{-4}$	$1.04 \pm 0.42 \times 10^{-2}$	$2.44 \pm 1.05 \times 10^{-2}$
	55213.5766	1.58×10^{-5}	1.40×10^{-4}	$5.07 \pm 2.11 \times 10^{-3}$	$1.14 \pm 0.56 \times 10^{-2}$
	55213.6428	2.38×10^{-5}	$1.59 \pm 0.75 \times 10^{-4}$	$8.53 \pm 3.49 \times 10^{-3}$	$1.86 \pm 0.82 \times 10^{-2}$
	55213.7089	◇	◇	$9.51 \pm 3.89 \times 10^{-3}$	$1.88 \pm 0.83 \times 10^{-2}$
	55213.7751	1.81×10^{-5}	1.47×10^{-4}	$5.51 \pm 2.29 \times 10^{-3}$	$1.20 \pm 0.58 \times 10^{-2}$
	55213.8413	1.89×10^{-5}	$1.96 \pm 0.89 \times 10^{-4}$	$8.11 \pm 3.33 \times 10^{-3}$	$1.75 \pm 0.78 \times 10^{-2}$
	55213.9736	3.28×10^{-5}	1.60×10^{-4}	$6.97 \pm 2.87 \times 10^{-3}$	$1.54 \pm 0.70 \times 10^{-2}$
	57738.0234	$7.38 \pm 3.01 \times 10^{-4}$	$9.60 \pm 3.90 \times 10^{-3}$	—	—

NOTE—Reflected sunlight has been removed from the measured magnitudes in Table 1. Cases where no measurement is available in NEOWISE are marked as “—”. Entries without uncertainties are 2σ upper limits.

^aModified Julian Date of the mid-point of the observation.

^bThermal flux density at W1.

^cThermal flux density at W2.

^dThermal flux density at W3.

^eThermal flux density at W4.

*Phaethon’s closest approach date to the Earth (2017-Dec-17). ◇Contaminated by a star.

Table 5. Temperature

Object	MJD ^a	W3/W4 ^b	T _{bb} ^c	T _{eff} ^d	T _{ss} ^e
			(K)	(K)	(K)
Phaethon	55203.2564	0.31±0.09	183	184 ⁺¹⁸ ₋₁₉	219 ⁺²¹ ₋₂₃
	55203.3888	0.29±0.08	183	180 ⁺¹⁶ ₋₁₈	214 ⁺¹⁹ ₋₂₁
	57035.2144	—†	241	236 [‡]	281
	57035.2801	—†	241	236 [‡]	281
	57035.4115	—†	241	236 [‡]	281
	57035.5429	—†	242	237 [‡]	282
	57035.6743	—†	242	237 [‡]	282
	57663.4184	—†	268	263 [‡]	312
	57663.5494	—†	267	262 [‡]	311
	57663.6149	—†	267	262 [‡]	311
	58024.3765	—†	201	197 [‡]	234
	58104.2148*	—†	277	271 [‡]	323
2005 UD	57750.3946	—†	238	233 [‡]	277
	58383.2977	—†	274	269 [‡]	319
	58383.4286	—†	274	269 [‡]	319
	58383.4941	—†	274	269 [‡]	319
	58821.4792	—†	265	260 [‡]	309
	58821.6099	—†	266	261 [‡]	310
	58821.7408	—†	266	261 [‡]	310
	58821.8716	—†	266	261 [‡]	310
1999 YC	55213.2458	0.43±0.25	218	208 ⁺⁴⁹ ₋₅₅	247 ⁺⁵⁸ ₋₆₅
	55213.5766	0.44±0.28	218	209 ⁺⁵⁴ ₋₅₉	249 ⁺⁶⁴ ₋₇₀
	55213.6428	0.46±0.28	218	214 ⁺⁵³ ₋₅₉	254 ⁺⁶³ ₋₇₀
	55213.7089	0.51±0.31	218	223 ⁺⁶⁰ ₋₆₄	265 ⁺⁷¹ ₋₇₆
	55213.7751	0.46±0.29	219	214 ⁺⁵⁵ ₋₆₁	254 ⁺⁶⁵ ₋₇₂
	55213.8413	0.46±0.28	219	214 ⁺⁵³ ₋₅₉	254 ⁺⁶³ ₋₇₀
	55213.9736	0.45±0.28	219	212 ⁺⁵³ ₋₅₉	252 ⁺⁶³ ₋₇₀
	57738.0234	—†	276	270 [‡]	322

^a Modified Julian Date of the mid-point of the observation.

^b Flux density ratio from Table 4.

^c Blackbody temperature calculated from $T_{bb}=278 \cdot R_h^{-0.5}$, where R_h (au) is from Table 1.

^d Effective temperature.

^e Subsolar temperature calculated from $T_{ss}=\chi^{0.25} \cdot T_{eff}$, where $\chi=2$ for observable asteroid hemisphere.

† No data available in NEOWISE. ‡ Assumed value calculated from $T_{eff}=0.98 \cdot T_{bb}$. * Phaethon's closest approach date to the Earth (2017-Dec-17).

Table 6. Dust Production Rate

Object	MJD ^a	M_d ^b (kg)	Q_{dust} ^c (kg s ⁻¹)
Phaethon	55203.2564	$< 6.9 \times 10^5$	< 0.18
	55203.3888	$2.9 \pm 1.5 \times 10^6$	0.77 ± 0.40
	57035.2144	n/a	n/a
	57035.2801	n/a	n/a
	57035.4115	n/a	n/a
	57035.5429	n/a	n/a
	57035.6743	n/a	n/a
	57663.4184	n/a	n/a
	57663.5494	n/a	n/a
	57663.6149	n/a	n/a
	58024.3765	$2.0 \pm 0.7 \times 10^6$	0.68 ± 0.24
	58104.2148*	$2.7 \pm 2.2 \times 10^4$	0.22 ± 0.18
2005 UD	57750.3946	$1.0^{+1.4}_{-1.0} \times 10^5$	$2.4^{+3.4}_{-2.4} \times 10^{-2}$
	58383.2977	$1.1^{+6.8}_{-1.1} \times 10^3$	$0.8^{+5.1}_{-0.8} \times 10^{-3}$
	58383.4286	n/a	n/a
	58383.4941	$1.5^{+7.1}_{-1.5} \times 10^3$	$1.1^{+5.2}_{-1.1} \times 10^{-3}$
	58821.4792	$1.8^{+61}_{-1.8} \times 10^2$	$6.9^{+230}_{-6.9} \times 10^{-5}$
	58821.6099	$2.2^{+8.0}_{-2.2} \times 10^3$	$8.5^{+31}_{-8.5} \times 10^{-4}$
	58821.7408	n/a	n/a
	58821.8716	n/a	n/a
1999 YC	55213.2458	$< 5.8 \times 10^5$	$< 8.8 \times 10^{-2}$
	55213.5766	$< 1.9 \times 10^5$	$< 2.9 \times 10^{-2}$
	55213.6428	$< 2.0 \times 10^5$	$< 3.0 \times 10^{-2}$
	55213.7089	◇	◇
	55213.7751	$< 1.5 \times 10^5$	$< 2.3 \times 10^{-2}$
	55213.8413	$< 1.6 \times 10^5$	$< 2.4 \times 10^{-2}$
	55213.9736	$< 3.2 \times 10^5$	$< 4.8 \times 10^{-2}$
	57738.0234	n/a	n/a

NOTE—The 2σ upper limit is represented with “ $<$ ”. A result of a negative value is expressed as “n/a”.

^aModified Julian Date of the mid-point of the observation.

^bDust mass from Equation (5).

^cDust production rate from Equation (6).

*Phaethon’s closest approach date to the Earth (2017-Dec-17). ◇Contaminated by a star.

Table 7. Optical Depth

Object	I_n^a (Jy)	I_d^b (Jy)	C_n^c (km ²)	C_d^d (km ²)	τ^e	$<\tau^f$
Phaethon	$8.5 \pm 0.6 \times 10^{-3}$	$3.7 \pm 1.0 \times 10^{-6}$	16.6 ± 3.9	$7.2 \pm 2.6 \times 10^{-3}$	$3.2 \pm 1.2 \times 10^{-9}$	7×10^{-9}
1999 YC	$2.2 \pm 0.1 \times 10^{-2}$	$5.4 \pm 2.7 \times 10^{-5}$	2.3 ± 0.5	$5.6 \pm 3.1 \times 10^{-3}$	$7.2 \pm 4.0 \times 10^{-9}$	2×10^{-8}

NOTE—From the *W*3-band.

^a Measured flux density scattered by the asteroid's cross sectional area.

^b Measured flux density scattered by the dust particles in the trail.

^c Cross section of asteroid calculated from Table 3.

^d Cross section of dust particles in the trail (Equation 7).

^e Optical depth.

^f Upper limit to the optical depth ($> 3\sigma$).

Table 8. Expectations for Dust Particle Encounters with DESTINY⁺ and the Dust Analyzer (DDA) on the Phaethon Mission

L^a (km)	Unit	a^b (μm)	M^c (kg)	N_1^d (m^{-3})	l_a^e (m)	N_{enc}^f
500	DESTINY ⁺	2300	1.0×10^{-4}	7.2×10^{-7}	110	1
	DDA	260	1.5×10^{-7}	5.7×10^{-5}	26	2
50,000	DESTINY ⁺	80	4.3×10^{-9}	7.0×10^{-9}	520	1
	DDA	9	6.1×10^{-12}	1.7×10^{-6}	84	6

NOTE—The characteristic interaction time T_{int} is 28 seconds at $L=500$ km and 2800 seconds at $L=50,000$ km, respectively.

^aDistance from Phaethon.

^bRadius of a dust particle.

^cMass of a dust particle.

^dNumber density of dust particles.

^eAverage separation distance between particles ($= N_1^{-\frac{1}{3}}$).

^fExpected number of dust particles to be encountered.

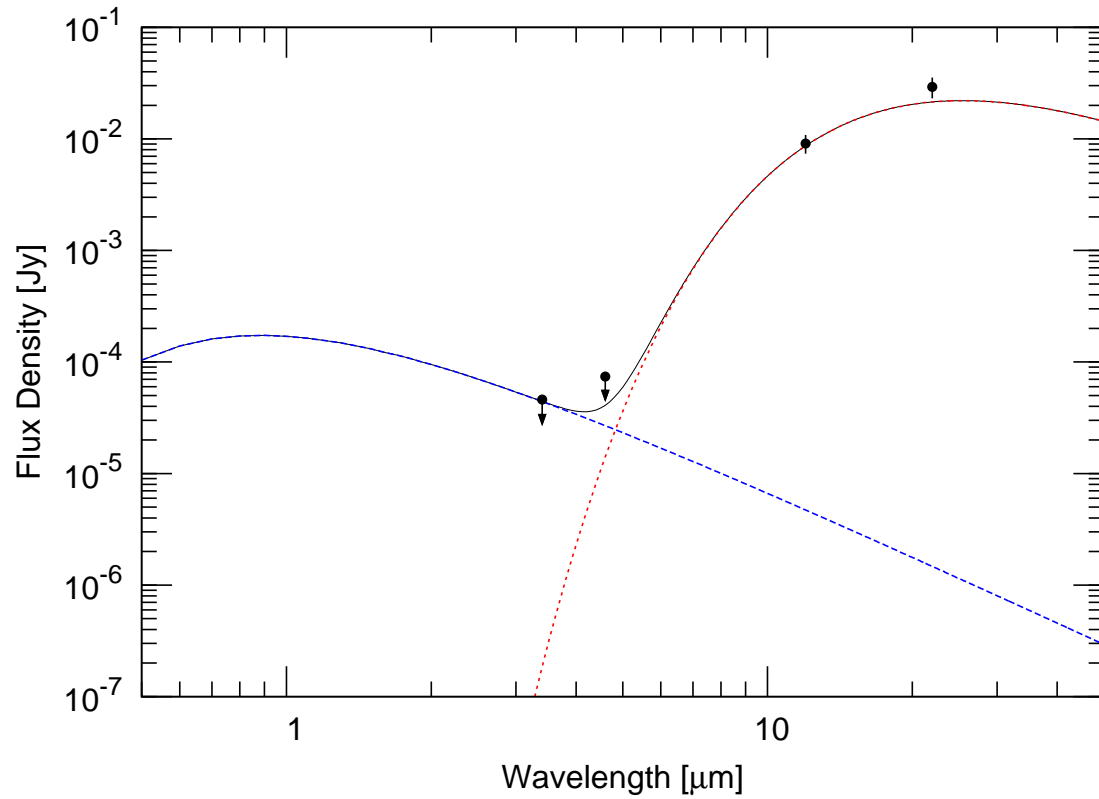


Figure 1. *WISE* observation of Phaethon on UT 2010 January 7 (MJD 55203.2564). The measured flux densities at the *W1* ($3.4\mu\text{m}$), *W2* ($4.6\mu\text{m}$), *W3* ($12\mu\text{m}$) and *W4* ($22\mu\text{m}$) are shown as points. The 2σ upper limit is represented with downward arrows. Reflected sunlight model (blue dashed-line), thermal model (red dashed-line) and combined signal (black solid-line) are over-plotted.

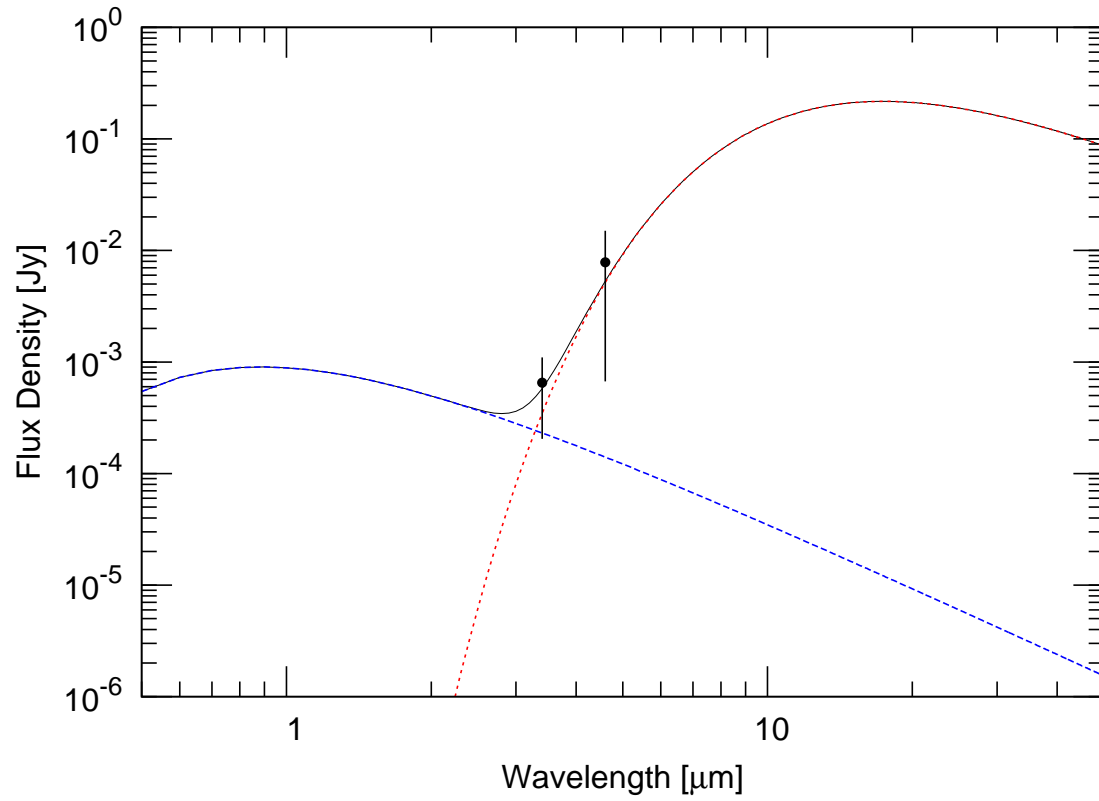


Figure 2. NEOWISE observation of 2005 UD on UT 2018 September 22 (MJD 58383.2977). Points show the measured flux densities at the *W1* ($3.4\mu\text{m}$) and *W2* ($4.6\mu\text{m}$). The model descriptions are same as Figure 1.

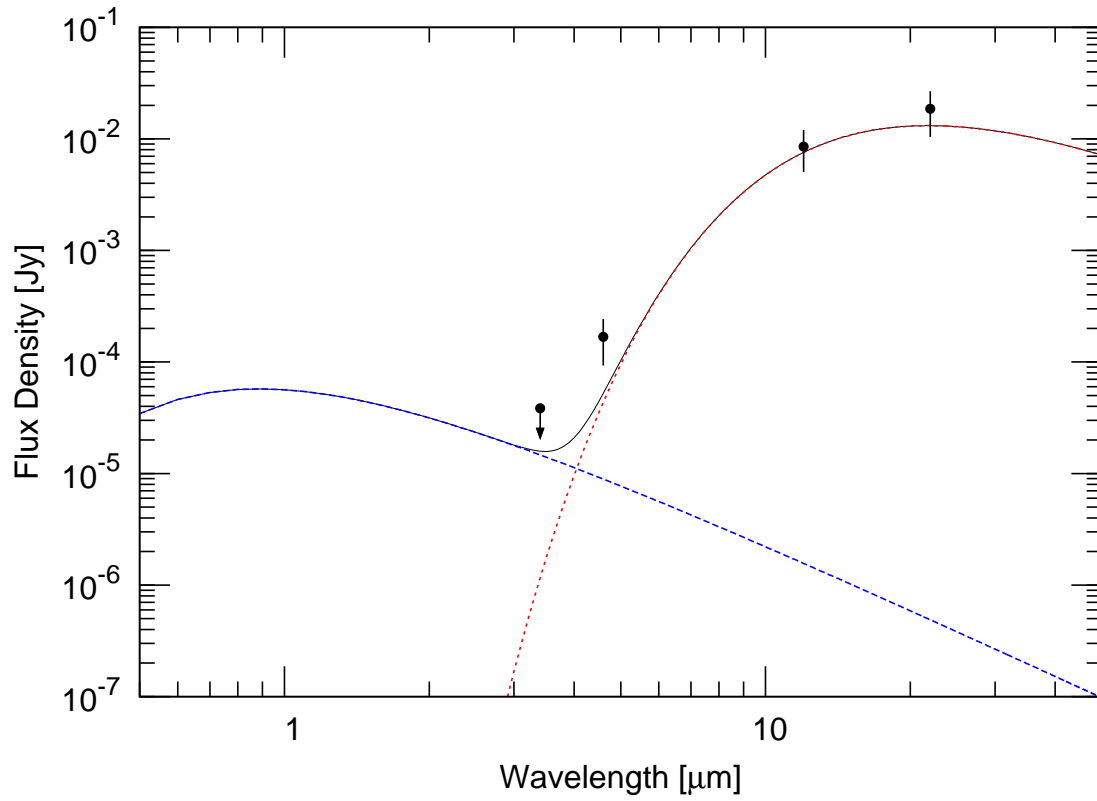


Figure 3. Same as Figure 1 but for 1999 YC observed on UT 2010 January 10 (MJD 55213.6428).

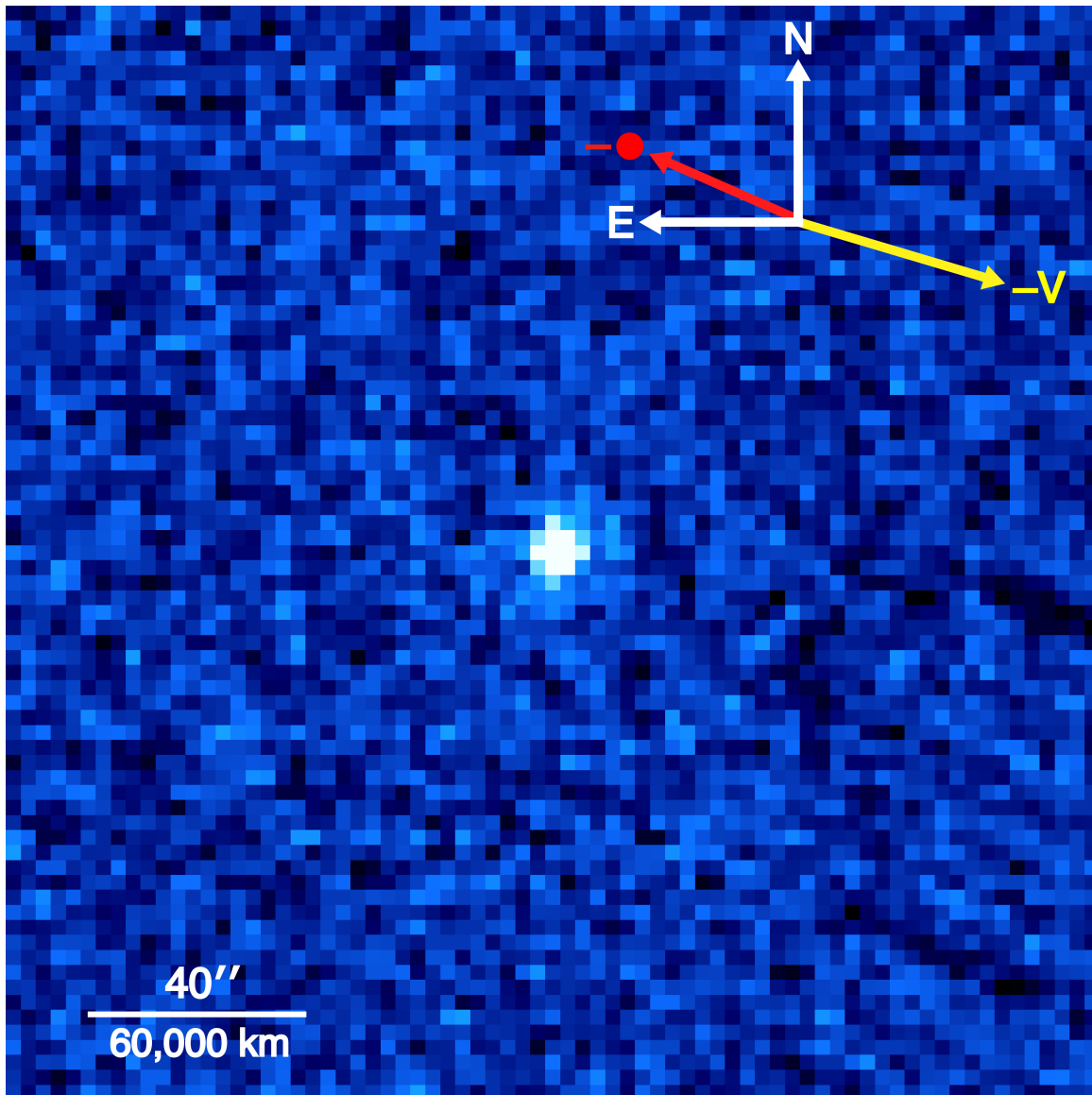


Figure 4. Composite *W3*-band image of Phaethon in 17.6 s integration (2×8.8 s) taken by *WISE* on UT 2010 January 7. The frame size is $200'' \times 200''$. No coma or tail is visible on the object having an FWHM of $7.8''$. Heliocentric, *WISE*-centric distances and phase angle were $R_h=2.32$ AU, $\Delta=2.08$ AU and $\alpha=25.1^\circ$, respectively. The cardinal directions (N and E), the direction of the negative heliocentric velocity vector ($-V$), and the anti-solar direction ($-\bullet$) are marked. A $40''$ scale bar corresponding to 60,000 km at the Δ distance to Phaethon is shown.

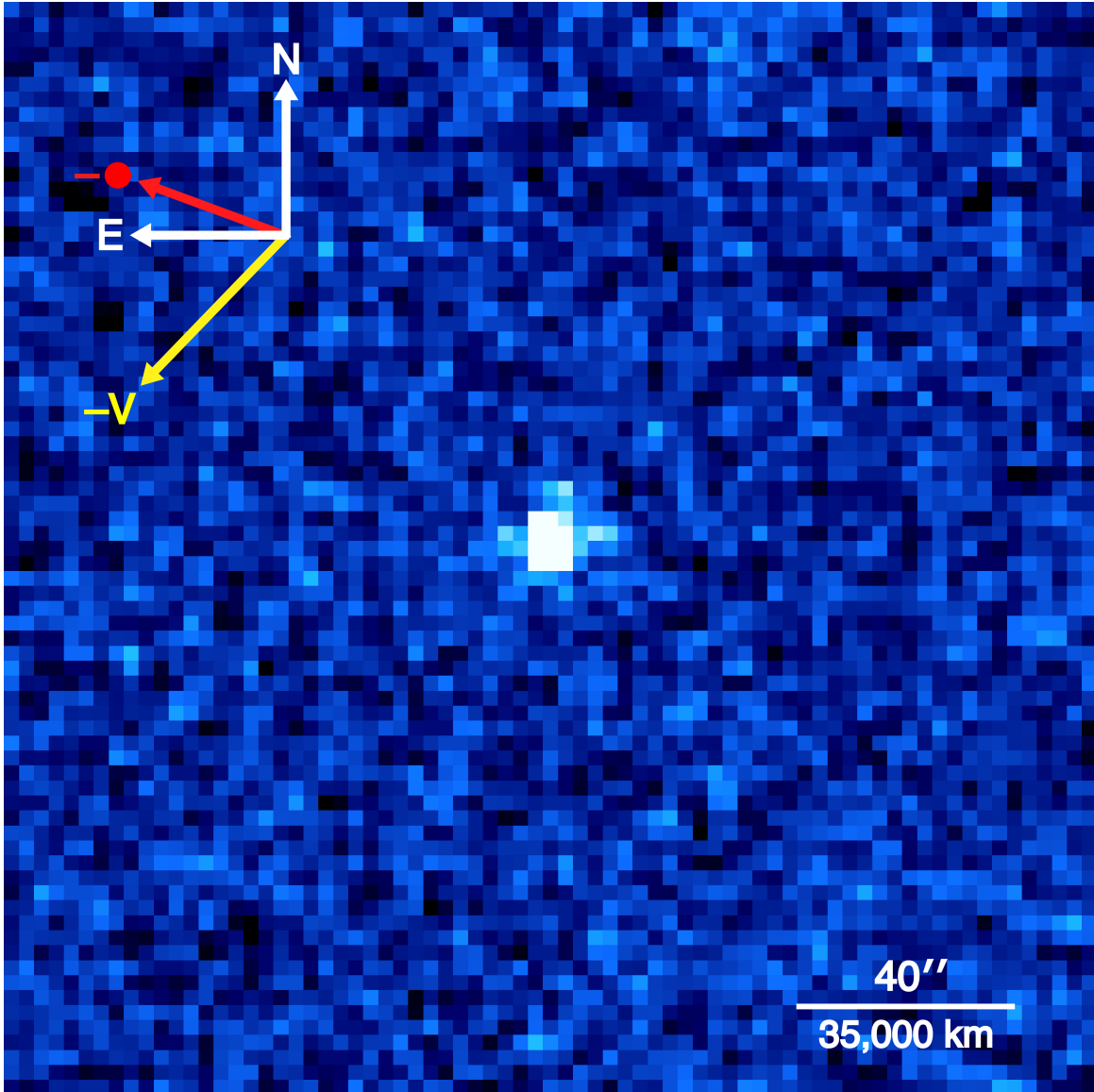


Figure 5. *WISE* W3-band image of 1999 YC on UT 2010 January 10 showing a point source with $\text{FWHM} \sim 7.1''$ in 35.2 s integration (4×8.8 s), centered in the frame of $200'' \times 200''$. $R_h = 1.62$ AU, $\Delta = 1.22$ AU and $\alpha = 37.3^\circ$. *N* and *E* exhibit the cardinal directions. $-V$ shows the direction of the negative heliocentric velocity vector and $-\bullet$ shows the anti-solar direction, respectively. A $40''$ scale bar corresponding to 35,000 km at the Δ distance to 1999 YC is shown.

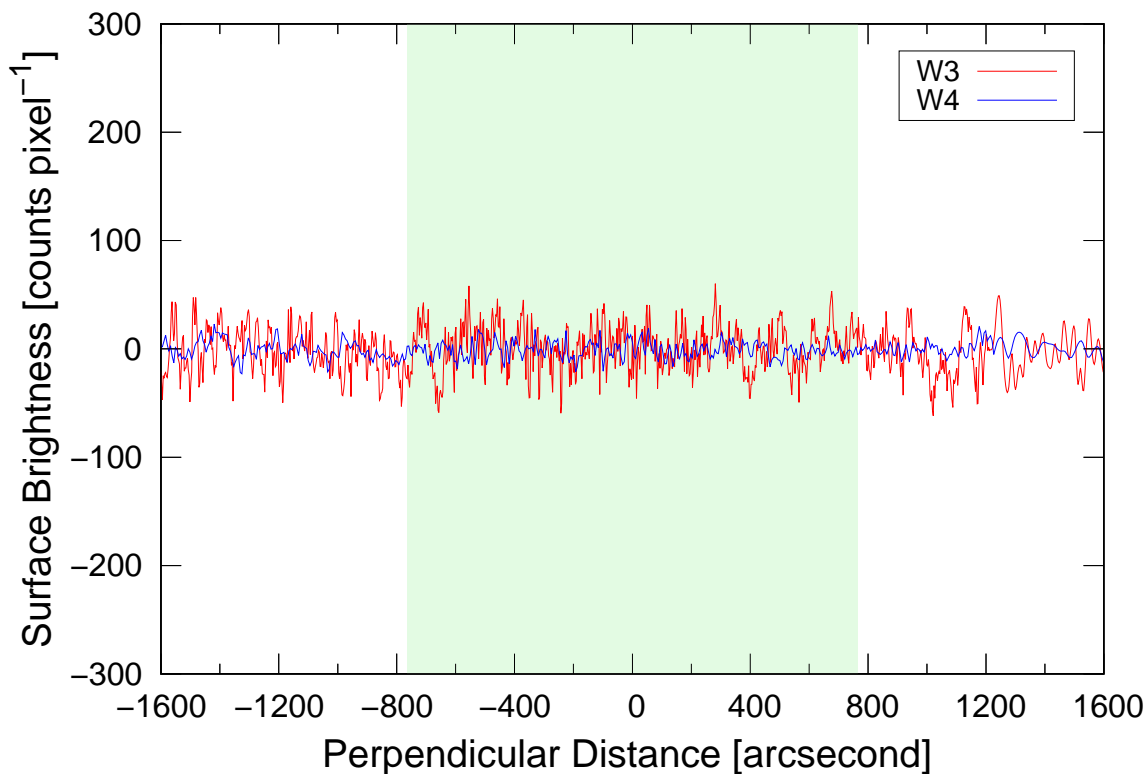


Figure 6. Averaged surface brightness cuts perpendicular to the projected orbital plane of Phaethon. Red and blue line shows a random cut measured in the $W3$ - and $W4$ -band at the expected trail location ($-V$), respectively. The $W3$ -band profile was obtained at distance $50''$ ($\approx 75,000$ km) from Phaethon while, in the $W4$ -band, the profile was extracted at distance $72''$ ($\approx 110,000$ km). The green region shows the expected location and approximate width of the in-plane dust trail. Surface brightness expressed in digital units (1 count per pixel) corresponds to $20.0 \text{ mag arcsec}^{-2}$ at $W3$ and $16.6 \text{ mag arcsec}^{-2}$ at $W4$.

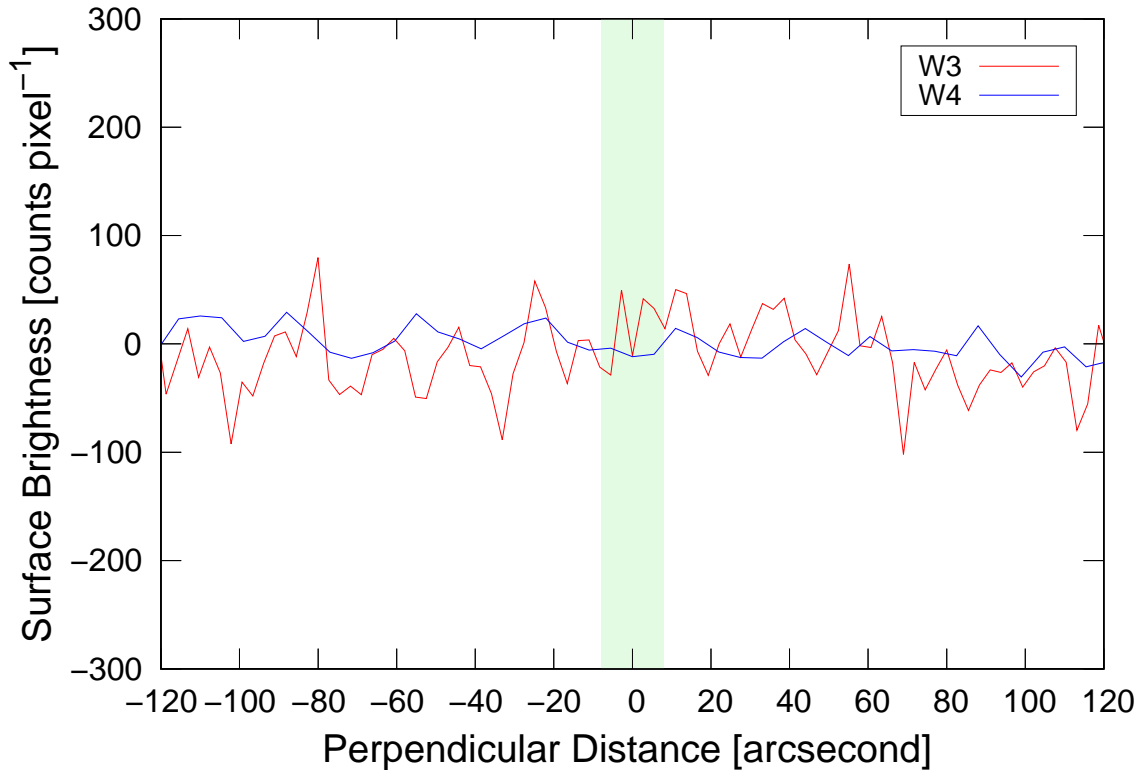


Figure 7. Same as Figure 6 but for 1999 YC. The *W3*-band profile is at distance 160'' ($\approx 140,000$ km) from 1999 YC and the *W4*-band profile is at distance 215'' ($\approx 190,000$ km).